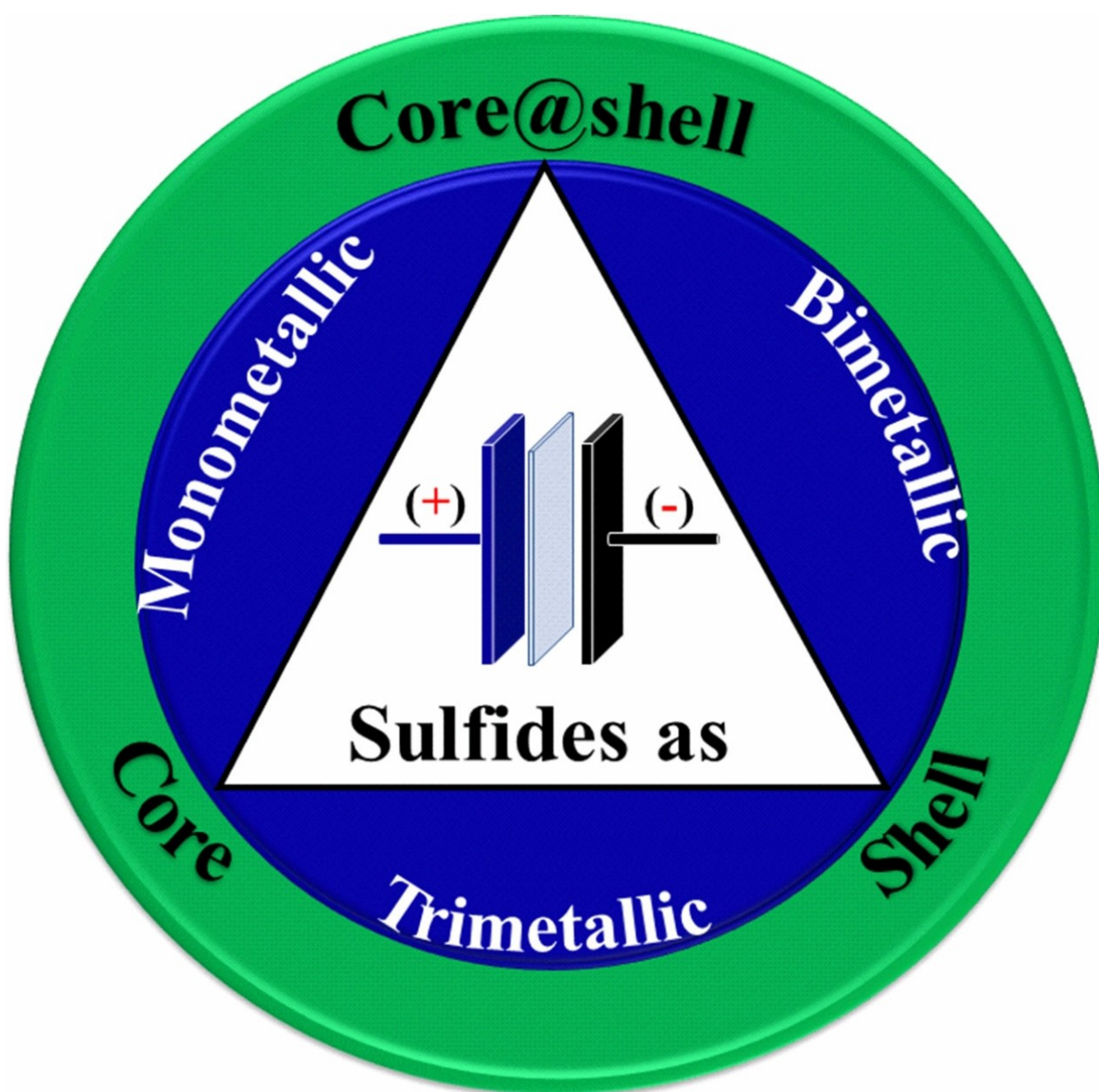


Recent Progress in Core@Shell Sulfide Electrode Materials for Advanced Supercapacitor Devices

Josué M. Gonçalves,^{*[a]} Matheus I. da Silva,^[a] Meisam Hasheminejad,^[a] Henrique E. Toma,^[a] Koiti Araki,^[a] Paulo R. Martins,^{*[b]} and Lucio Angnes^{*[a]}



Highly conductive and surface area complex hierarchical 3D core@shell nanostructures made of multi-metallic multi-valence sulfides are being specially designed as electrode materials of high performance and high power supercapacitors. In fact, bimetallic and trimetallic sulfides have outstanding redox properties as compared with the corresponding single-phase sulfide based materials, and much higher electrical conductivity than the analogue oxide materials, being excellent materials for the design of core@shell structures with exceptional charge capacity, power, and energy performance. For this purpose, the core material should exhibit high charge diffusion rates and large specific capacitance, while the shell should improve the surface area by promoting a greater accessibility to the electro-

active sites thus maximizing the charge capacity and conductivity. In this context, a rational design of nanostructured materials encompassing advanced 2D materials (such as graphene, MXene, black phosphorus, transition metal hydroxides, etc.), as well as carbon materials such as CNTs and carbon cloth, seems to be a very promising strategy to realize flexible enough electrode materials for the development of wearable devices, self-charged energy storage devices and microsupercapacitors. In all cases, multi-metallic sulfide-based core@shell materials play a key role as electroactive materials for realization of high performance, portable and flexible energy storage devices paving the way to a more advanced and sustainable society.

1. Introduction

The rapid development of society and the worldwide increase in energy consumption demand strategic research on renewable energy and sustainable energy storage technologies, in order to overcome the threats from climate changes and the irreversible depletion of fossil fuels.^[1] In this sense, efforts have been made for the development of electrode materials and their microstructure design,^[2] including the electrochemical lithium-ion batteries (LIBs), and emerging devices like the supercapacitors (SCs).

Among the materials used in battery electrodes, metal oxides, hydroxides and sulfides have been increasingly studied as positive electrodes of hybrid supercapacitors, showing a great potential in the development of new high-performance devices. For instance, Gonçalves *et al.*^[3] showed that transition bi- and trimetallic oxides/hydroxides and multicomponent systems can exhibit exceptional performances as electrode materials introducing great perspectives for hybrid energy storage devices. In particular, Cheng and co-workers^[1] reviewed the recent progress of core-shell composites using NiCo_2O_4 as scaffolds, and of shell materials based on metal oxides, hydroxides, sulfides as well as conductive polymers.

Transition metal sulfides are gaining prominence as advanced materials for electrochemical supercapacitors due to their outstanding properties, including good electrical conductivity, high specific capacity, low electronegativity, unique crystal structures, and high redox activity.^[4] In this context, several review papers have been published highlighting the energy storage properties of materials such as MoS_2 (2015,^[5]

2017)^[6] and NiCo_2S_4 (2017),^[7] as well as more comprehensive topics.^[8] For example, Kulkarni *et al.* (2017)^[9] have summarized the synthetic methods for obtaining nanostructured metal sulfides, showing their application in energy conversion and storage devices. More recently, Yu and co-workers (2018)^[10] reviewed the rational design and preparation of several micro/nanostructures based on mixed metal sulfides (MMS) with controlled morphologies, sizes, and compositions for energy storage devices such as LIBs, sodium-ion batteries (SIBs), hybrid supercapacitors (HSCs) and metal-air batteries (MABs), and for application as catalysts in the water splitting reaction. On the other hand, Geng *et al.*^[11] have focused their attention on the preparation of transition metal sulfide composites with graphene or graphene derivatives, exploring the strategies for morphologic control and their applications in LIBs, SIBs, and SCs.

Inspired by the work of Cheng and co-workers^[1] on core-shell composites encompassing NiCo_2O_4 scaffolds, and on the advances in transition metal sulfides, hereon we present a critical review on the design of core@shell structure sulfides as electrode materials for advanced HSCs. Firstly, we will summarize the types of core@shell structures reported in the literature in order to provide the fundamental concepts; followed by the discussion on the electrochemical signature of supercapacitor and battery type materials. Then we will comment on the most recent advancements in electrode materials for HSCs based on metal sulfides. They were subdivided into mono, bi and trimetallic sulfides, and employed in the design of electrode materials encompassing specific roles as core, shell or both. Finally, the perspectives and future directions will be presented.

[a] Dr. J. M. Gonçalves, M. I. da Silva, Dr. M. Hasheminejad, Prof. H. E. Toma, Prof. K. Araki, Prof. L. Angnes
Instituto de Química
Universidade de São Paulo
Av. Prof. Lineu Prestes 748, 05508-000 São Paulo-SP, Brazil
E-mail: josuemartins@usp.br
luangnes@iq.usp.br

[b] Prof. P. R. Martins
Instituto de Química
Universidade Federal de Goiás
Av. Esperança s/n, 74690-900 Goiânia-GO, Brazil
E-mail: pauloqmc@ufg.br

2. Core@Shell Materials and their Use as Energy Storage Systems

Core@shell structures can be designed by combining two materials with different intrinsic properties, wherein the core material is surrounded by a second type of material providing the shell.^[12] In fact, an enormous variety of core@shell materials

with different composition, morphology, properties, and applications have been prepared.^[13] In order to better distinguish all the possible systems in as clear as possible way, a newly expanded classification is being employed in this account, where the term "core@shell nanomaterials" is used as a synonym for "encapsulated structures" thus encompassing core@shell, yolk-shell/hollow structures and sandwiched core-shell structures,^[13] as shown in Figure 1. Nevertheless, it is important to point out at this point that some composites are mistakenly being described as core@shell materials in the literature, thus causing confusion in significant extent.



Josué Martins Gonçalves is a postdoctoral researcher in the group headed by Prof. Lucio Angnes at University of São Paulo (USP), Brazil, and honored with a prestigious research fellowship from FAPESP. He graduated in Chemistry at University Vale do Acaraú (UVA) in 2014 and received his Ph.D. degree from USP in 2019, under supervision of Prof. Koiti Araki. His current research interests include applications of nanomaterials for use in sensors, electrocatalysis, and energy conversion and storage devices.



Matheus Ireno da Silva received his B.Sc. in Chemistry from the Federal Institute of Education, Science and Technology of São Paulo (IFSP), Brazil, in 2017. Currently, he is a Natural Sciences Ph.D. student at the Institute of Chemistry of University of São Paulo (IQ-USP) Brazil, with emphasis in Nanotechnology and Supramolecular Chemistry. His research interests are focused on the synthesis, characterization, and application of self-assembled nanoparticles and nanocomposites, aiming the improvement of their sensing, electro and photocatalytic and energy storage, production and conversion performances by synergistic effects.



Meisam Hasheminejad is a postdoctoral researcher supported by FAPESP at the University of São Paulo (USP), Brazil. He received his Ph.D. in 2017 from Nanjing University, China. He pursued postdoctoral studies with Prof. Majid Mohseni at Shahid Beheshti University in September 2017. He received support from Iran's National Elites Foundation and then joined the research group of Prof. Thomas A. Klar at Johannes Kepler University Linz in Austria as a visiting scholar. His current research involves surface plasmon resonance microscopy and electrochemistry.



Henrique Eisi Toma holds a Ph.D. in Chemistry and is Professor at the University of São Paulo. He is Guggenheim Fellow, Member of the Brazilian Academy of Sciences, TWAS and Grã-Cruz of the National Science Order. His major interests are inorganic, bioinorganic, supramolecular chemistry, and molecular nanotechnology.

2.1. Core@Shell Electrode Materials for Energy Storage Systems

For energy storage systems, the most desired properties are a high electrical conductivity and a high capacitance/electrochemical activity, which are characteristic of high-energy and high-power density materials. Morphology control can be explored to maximize the surface area, while ion diffusion and density of redox sites will play key roles. Accordingly, core@shell structures such as nanowire-nanosheet^[14] and nanotube-nanosheets^[15] have been intensely investigated in recent years.



Paulo Roberto Martins received his Ph.D. degree from Institute of Chemistry of University of São Paulo in 2012, under the guidance of Professor Koiti Araki. Currently, he is Assistant Professor at the Federal University of Goias, Brazil. His research interests are focused on development of new materials based on layered double hydroxides for energy storage purposes.



Koiti Araki is full professor at Institute of Chemistry of University of São Paulo since 2006, principal researcher of the Supramolecular Chemistry and Nanotechnology Lab, member of São Paulo State Academy of Science, and coordinator of SisNANO-USP. His research interests are focused on the design and preparation of functional hybrid nanobiomaterials and nanocomposites by co-ordinative supramolecular chemistry approach that can help tackling the main challenges in energy, nanomedicine, and environment.



Lucio Angnes is a full professor at Institute of Chemistry of University of São Paulo. His research interests include the construction of electrodes with new and alternative materials, development of modified electrodes, arrays of microelectrodes, design different procedures of enzymes immobilization (on electrodes or inside microchannels) and association of the created devices with flowing systems (flow and batch injection analysis). He is a member of the São Paulo State Academy of Science.

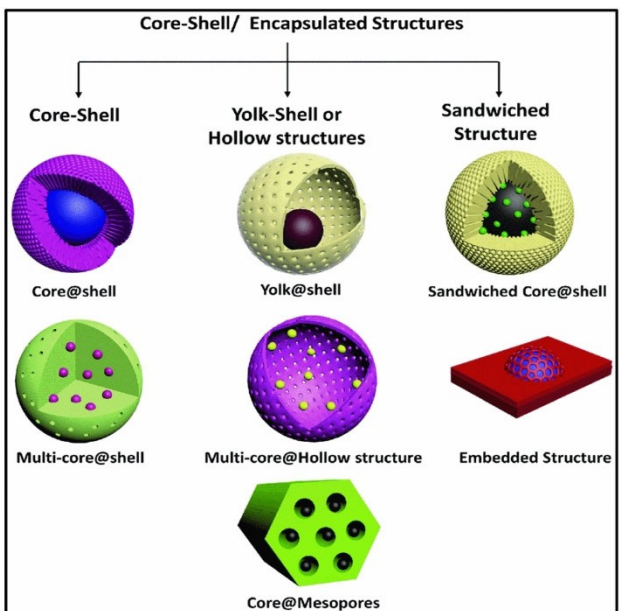


Figure 1. Schematic illustrations showing the different types of core-shell structures classified according to their morphology. Reproduced from Ref. [13] under the terms of the Creative Commons License. Copyright (2020) The Authors.

In fact, synergistic effects associated with the core@shell structures can improve the energy storage capacity and enhance the power density of electrode materials when compared to the structure of a single material. For example, Zhang and colleagues^[16] prepared two types of $\text{NiCo}_2\text{O}_4@\text{NiMoO}_4$ hierarchical core@shell nanostructures, in which NiCo_2O_4 behaves as scaffold in form of uninterrupted nanosheet arrays (UNSA, Figure 2A) or nanoneedle arrays (NNA, Figure 2B), and NiMoO_4 forms hierarchical nanosheet structures, and investigated the electron transport properties of the resulting electrode materials. Interestingly, the energy stored by NiCo_2O_4 -UNSA@ NiMoO_4 electrodes was 22–39% larger than of NiCo_2O_4 -NNA@ NiMoO_4 at various current densities. Furthermore, the NiCo_2O_4 -UNSA@ NiMoO_4 electrodes delivered current with a superior rate capability than the ones based on NiCo_2O_4 -NNA@ NiMoO_4 . Such improved energy storage properties were attributed to the best characteristics of the NiCo_2O_4 -UNSA@ NiMoO_4 electrode, such as more favorable transport channels for electrons (Figure 2C), enhanced reversibility, and lower charge-transfer resistance than the NiCo_2O_4 -NNA@ NiMoO_4 electrodes. The uninterrupted porous network formed by tight interconnection between NiCo_2O_4 nanosheet scaffolds and the large lateral size are crucial for the optimization of electrochemical performances, as confirmed by theoretical simulations and electrochemical impedance spectroscopy. In short, core@shell structures are being eagerly pursued as electrode materials in high performance energy storage systems, as it will be discussed in the following topics.

3. “Supercapacitive” and “Battery”-Type Materials: Typical Performances and Devices

Due to the increasing current need for high energy and high-power density storage systems, devices combining the high energy capacity of batteries with the power density of conventional capacitors have been pursued. For this purpose, new supercapacitive and battery type materials have been studied and significant advancements have been achieved in the recent years.

The electrical double-layer capacitors (EDLCs) store energy based on the ion migration induced by the electric field and formation of an electric double-layer on high surface area conductors (Figure 3A).^[17] This is the case of carbonaceous materials such as graphene and carbon nanotubes. As shown in Figure 3B–3C, the electrochemical signature of EDLC material in cyclic voltammetry (CV) is characterized by a rectangular-box-type profile, while the Galvanostatic Charge/Discharge (GCD) curves show a symmetric triangular pattern.^[18]

The second class of capacitive materials are the pseudocapacitive ones. The most widely used pseudocapacitor materials are RuO_2 and MnO_2 . This type of materials features a combined mechanism to deliver an electrochemical response resembling that of capacitive materials. They store charge *via* Faradaic processes (by accessing two or more redox states of the metal centers in the materials, e.g., Mn(III) and Mn(IV) oxides, and *via* non-Faradaic processes associated with the formation of an electrical double layer concomitantly with the redox processes (Figure 3D),^[17] showing similar electrochemical signatures (CVs and GCD profiles) of EDLC,^[18] indicative of rapid faradaic reaction that are not limited by solid state diffusion^[19] (Figure 3E–3F), justifying the denomination “pseudocapacitance” to label the energy stored in such materials.

In contrast, due to the phase rule, battery-type materials such as $\text{Ni}(\text{OH})_2$, exhibit quite different behavior as compared to supercapacitive materials since the potential remains more or less constant during the charging-discharging processes, as shown in Figure 3G. In addition, the couple of well-defined redox peaks in the CVs and the plateau in the GCD profiles are characteristic of materials with solid-state diffusion-controlled faradic reactions (Figure 3H–3I).

It is also important to note that the metric used to evaluate the performance of supercapacitive and battery-type materials is also different. While, the specific capacitance is given in Fg^{-1} , the energy stored in battery-type materials ought to be presented as specific capacity (mAhg^{-1}) or specific charge (Cg^{-1}).

As mentioned before, the development of supercapacitor devices is a very promising alternative, since they can offer high energy-storage capacity with very high power outputs.^[18] These devices can be classified into three types: a) symmetric, b) asymmetric or c) hybrid supercapacitors. Both electrodes in symmetric devices are made of the same supercapacitive electrode material; for example, the cathode and anode can be made of graphene (graphene//graphene). In contrast, the denomination asymmetric supercapacitor should only be used

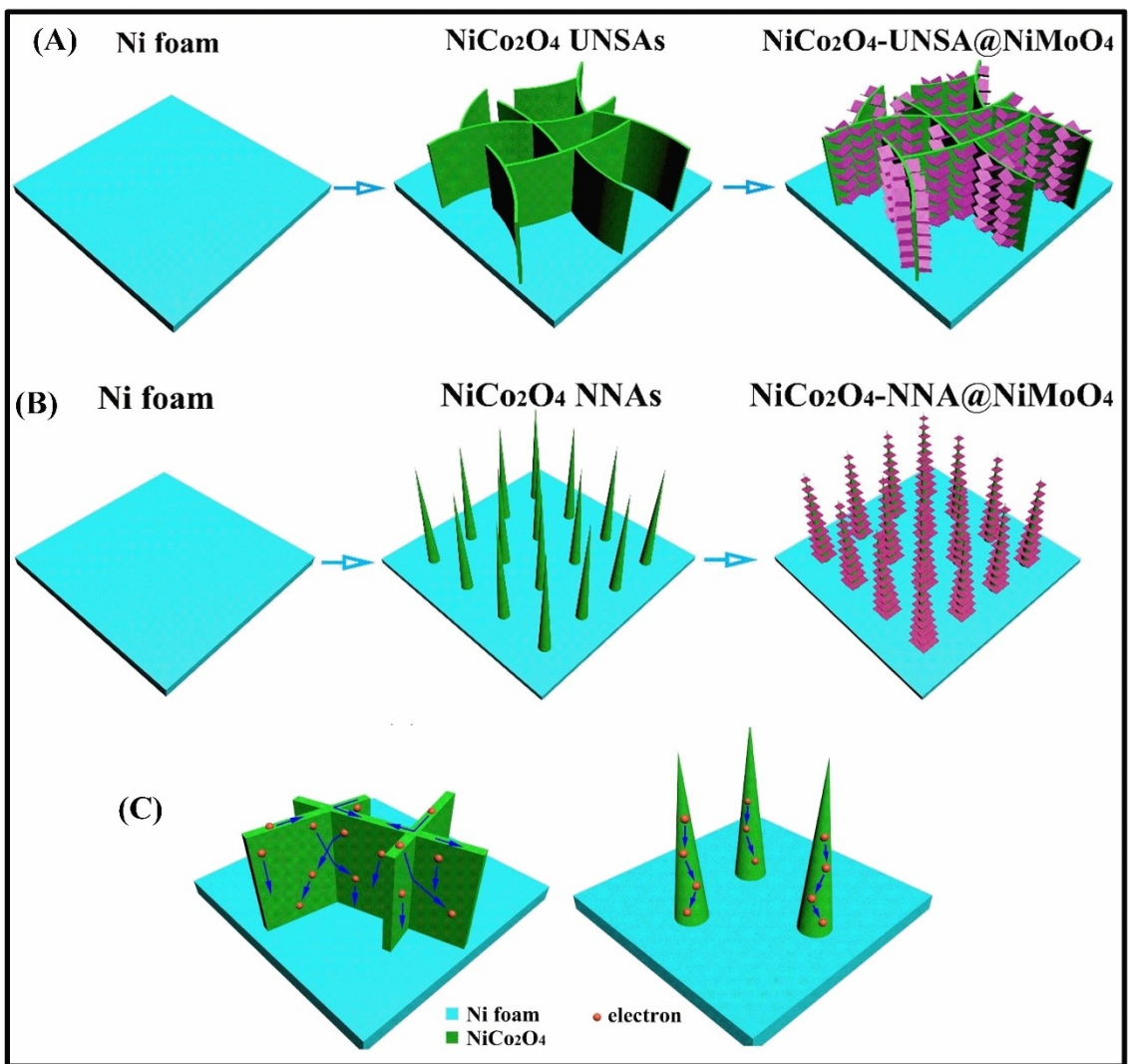


Figure 2. Schematic illustration of the two-step synthesis of (A) NiCo₂O₄-UNSA@NiMoO₄ and (B) NiCo₂O₄-NNA@NiMoO₄ directly on Ni foam. (C) Schematic illustration of electron transport channels in UNSA and NNA 3D electrodes. Reproduced from Ref. [16] with permission. Copyright (2016) Elsevier B.V.

when the device is made of two different capacitive or pseudo-capacitive electrode materials (EDLC//pseudo-capacitive) are respectively used in the cathode and the anode, for example, activated carbon//RuO₂), or with electroactive materials having different proportions of the redox-active sites.^[18] The most interesting combination in order to get unsurpassed energy density, however, is by uniting electrode materials with different charge storage mechanisms to assemble hybrid supercapacitors, for example, one capacitive or pseudo-capacitive and one battery-type faradic electrode material,^[18] such as in graphene//Ni(OH)₂ and MnO₂//Ni(OH)₂ devices.

In fact, the preparation of hybrid devices can result in greatly advantageous, since they can deliver simultaneously both high power and high-energy characteristics (Figure 4A), with an electrochemical signature in between SC and battery-type electrodes in addition to a wider working voltage. However, some intrinsic characteristics of the battery-type electrode generally persist as drawbacks, such as slow charge kinetics, which leads to poor rate performance, inferior life

cycle and sluggish dynamics.^[18] Generally, though, the asymmetric supercapacitor will be able to provide the required high working voltage with high energy density at high power rates and long-standing driving stability,^[18] and the typical CVs and GCD curves of these devices will show negligible redox peaks and plateaus, respectively^[19] (Figure 4B).

At this point, it is important to remember that metal sulfide materials are considered to be battery-type materials, although in many articles they are classified as supercapacitive materials, and their devices as symmetric/asymmetric supercapacitors. These classification were recognized as not being correct and several review articles were recently published trying to clarify and avoid further dissemination of that misconception in the literature.^[17–18,20]

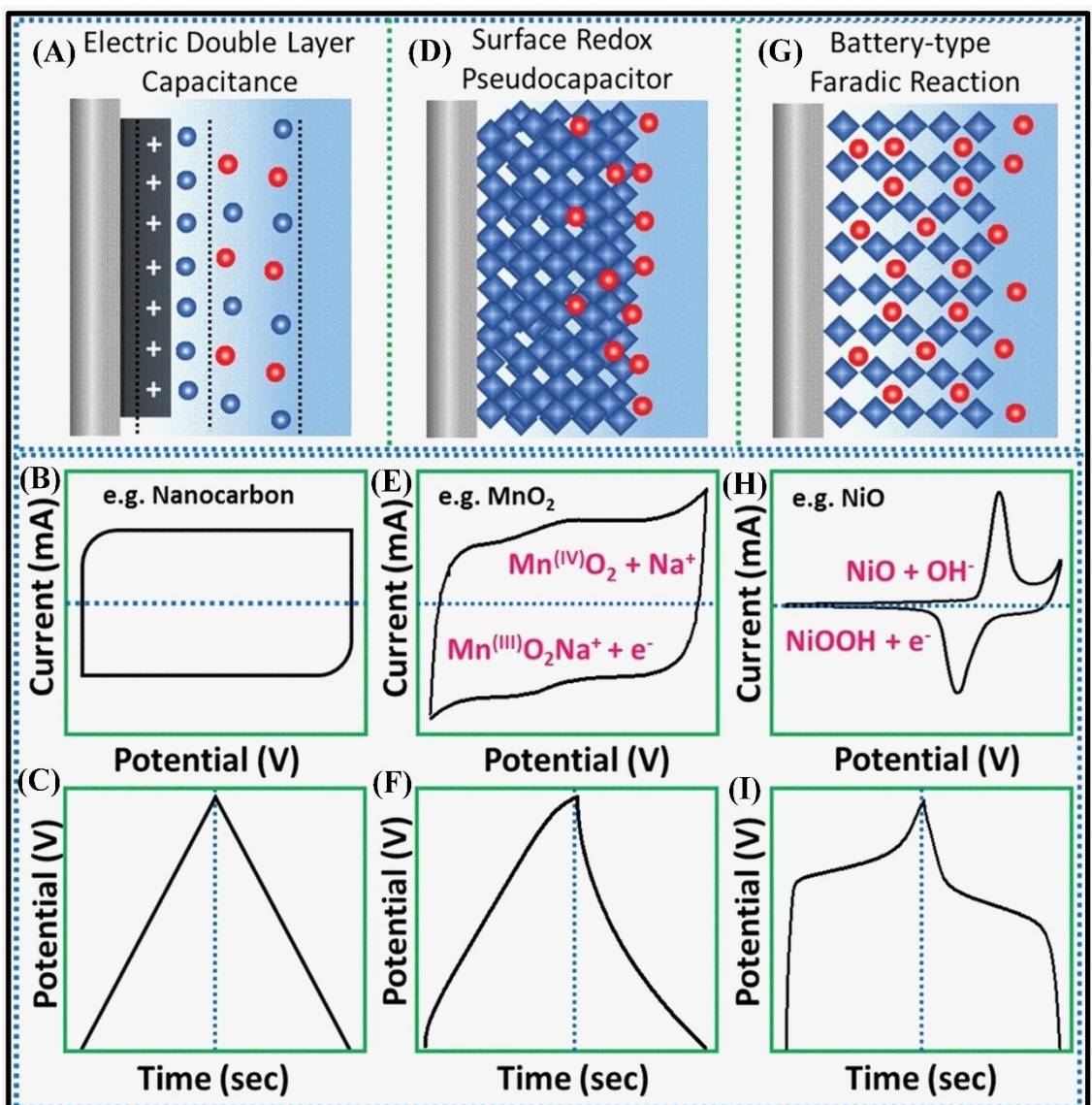


Figure 3. The energy storage mechanisms with their corresponding representative CV and CD curve profiles: A–C) electrical double-layer capacitance, D–F) surface redox capacitance and G–I) faradic battery-type material. Reproduced from Ref. [18] with permission. Copyright (2020) Wiley-VCH GmbH.

4. Monometallic Sulfides in Core@Shell Structures

Many manufacturers, particularly those focused on high energy consumption goods and processes, such as the automobile industries and fuel producers, are seeking for devices with the highest as possible power and energy density. Poor electrical/ionic conductivity is a problem that affects the kinetics of electrochemical reactions impairing the performance of energy storage devices. Accordingly, many efforts have been made to improve the charge-transfer kinetics, as well as to increase the voltage window and capacity of electrode materials. Hetero-nanostructured materials can provide an effective solution by increasing the concentration of active sites which could boost the surface reaction kinetics and improve electrical conductivity.^[21] The principle is the use of two mixed transition

metal oxides such as MnCo_2O_4 , NiMn_2O_4 , CoFe_2O_4 , and NiMoO_4 in which one material provides redox states increasing the energy capacity while the second one confers enhanced conductivity. This synergistic effect and combined behavior could lead to the improvement of capacitance and robustness.^[22]

Despite the progress observed for supercapacitor devices based on mixed transition metal oxides, the actual energy capacity is yet much lower than the theoretically predicted one. To improve the practical capacity, the hetero-nanostructured materials are being combined with other materials such as metal sulfides. In fact, metal sulfides such as NiS_x , CoS_x , and MoS_2 can be immobilized on the surface of transition metal oxides to form core@shell nanostructures.^[23] Monometallic sulfide core@shell nanostructures can be used either as core, shell, or both. These three types of nanostructured materials will be described in the next sections.

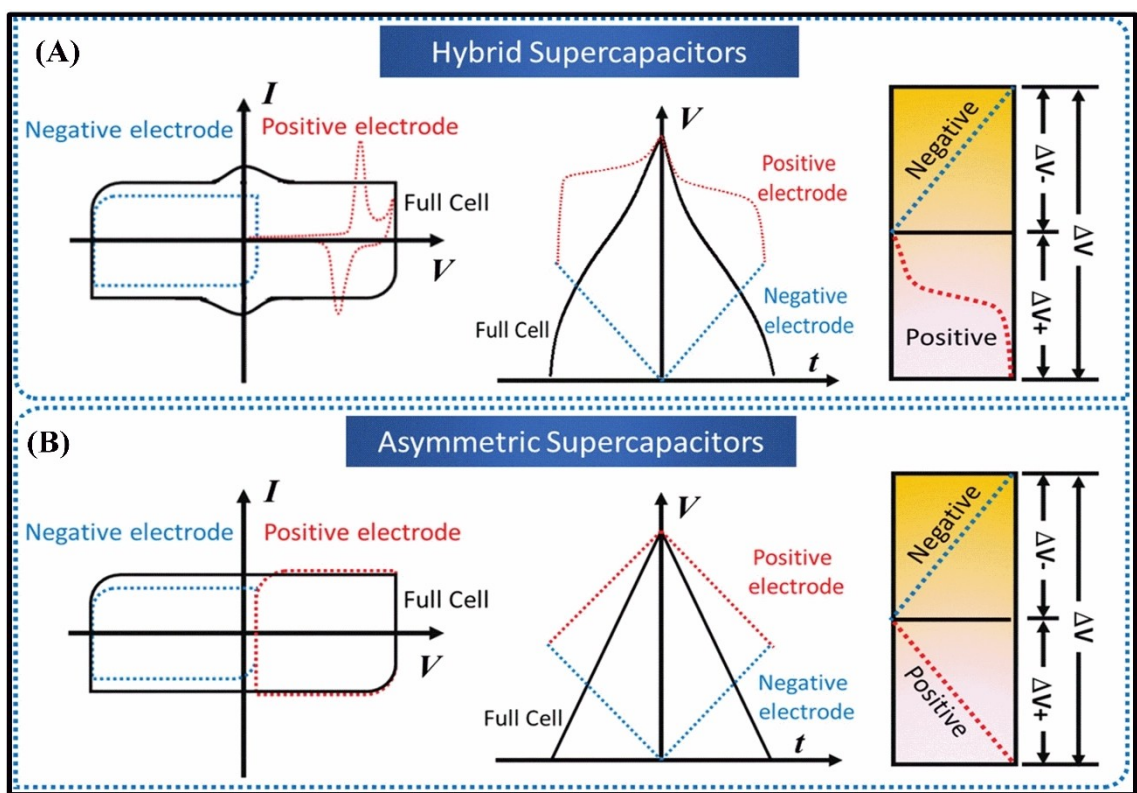


Figure 4. Differences of the electrochemical signature of a typical A) hybrid and B) asymmetric supercapacitor. The electrochemical features of their corresponding electrodes are also included to improve the clarity. Reproduced from Ref. [18] with permission. Copyright (2020) Wiley-VCH GmbH.

4.1. Monometallic Sulfides as Core Materials

Materials with different morphologies and dimensionality have been reported as electrode materials. Among them, 1D nanowires, 2D nanosheets, and 3D hollow spheres have been extensively examined. The conventional method to fabricate core@shell systems from mono to trimetallic core@shell structures is by the hydrothermal growth of metal sulfides. Song and co-workers^[23] used this technique to functionalize nickel-based sulfides/mesoporous silica complexes with boron nitride (BN) and carbon. They used different hydrothermal

reaction times (3, 5, 7, 9, 12, 18, and 24 h) to obtain materials with different morphologies. They showed that by increasing the reaction time from 5 to 9 h a rod-like structure with mesoporous silicon distributed on the surface was obtained. But the material with such a morphology started to disappear after 12 and 18 h of reaction, and a spherical shaped material containing small mesoporous silica particles was formed after 24 h. The scheme in Figure 5A shows the formation of $\text{mSiO}_2@\text{NiS}_2$ and $\text{mSiO}_2@\text{NiS}$ at 600°C , while their respective SEM images are shown in Figures 5B and 5C. The specific energy capacity of $\text{mSiO}_2@\text{NiS}_2$ was 449.7 F g^{-1} at 1 A g^{-1} , and

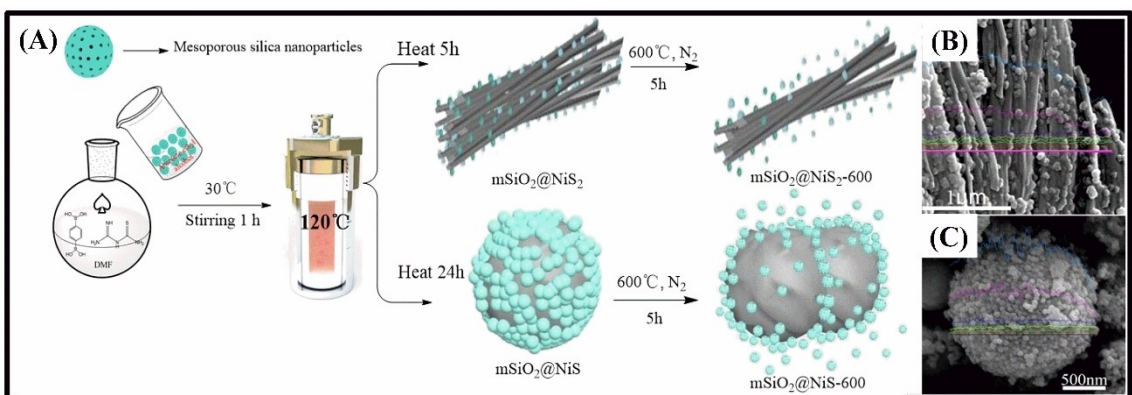


Figure 5. Schematic illustration of the steps of $\text{mSiO}_2@\text{NiS}_2$ and $\text{mSiO}_2@\text{NiS}$ formation and their respective SEM images (A) and (B). Reproduced from Ref. [23] with permission. Copyright (2020) Elsevier B.V.

the energy density 202.5 Wh kg^{-1} at a power density of 959.2 W kg^{-1} , quite high values especially considering the 200% enhancement of the capacitance retention after 8000 cycles at 20 A g^{-1} . The ultrahigh-energy density and power density of $\text{mSiO}_2@\text{NiS}_2$ as compared with NiS_2 and $\text{mSiO}_2@\text{NiS}$ was attributed to its unique morphology and nanostructuration. The mesoporous silica enhanced the stability of the system to cycling while the addition of boron nitride and carbon improved the conductivity and energy capacity of the nanostructured material.

In addition to nickel sulfides, other metal sulfides have also been used as core material in the preparation of hierarchical core@shell structures. Cobalt sulfides (Co_xS_y) have attracted attention in monometallic materials because of their high capacitance, high rate capability, and excellent cycling stability.

However, the application of such materials is limited by the poor electrical conductivity and mechanical stability of cobalt sulfide.^[24] To solve this problem, Trabizi *et al.*^[25] combined it with reduced graphene oxide using an one-pot hydrothermal method to get the rGO-cobalt sulfide (rGO- Co_3S_4) nanocomposite. rGO was prepared by reduction of GO (from natural flake graphite) and used for the preparation of PANI/rGO- Co_3S_4 nanocomposite by *in situ* chemical polymerization of aniline on the rGO- Co_3S_4 particles. Figure 6A shows the scheme of the fabrication process and TEM images of the components (Figure 6B–6D). In fact, it can be observed that the rGO with Co_3S_4 nanoparticles anchored on the surface acts as a substrate for deposition of PANI nanostructures.^[25]

The CV curves show that PANI/rGO- Co_3S_4 provides the highest current density (Figure 6E) and specific capacitance

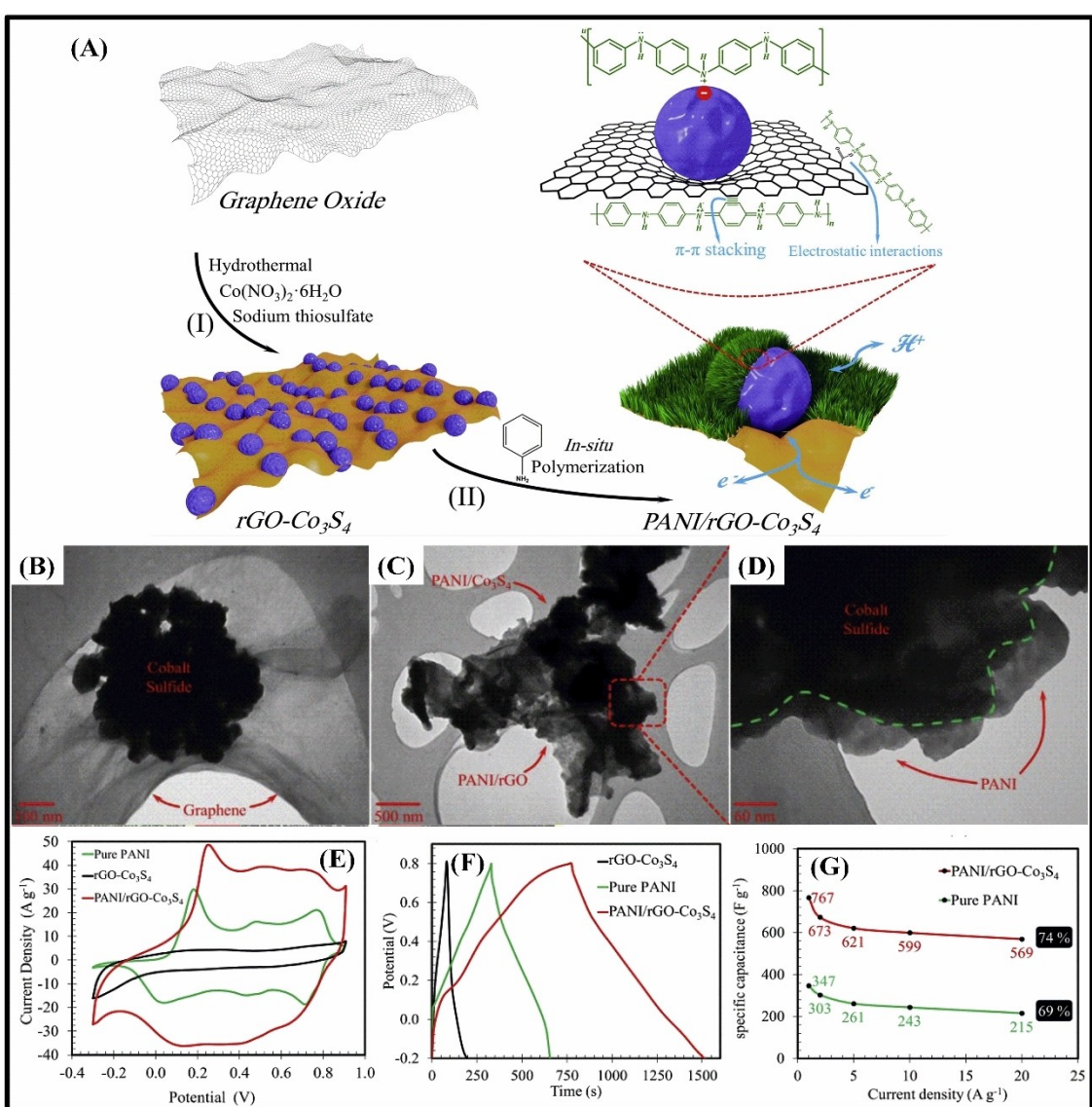


Figure 6. Scheme of the PANI/rGO- Co_3S_4 nanocomposite fabrication process (A), and TEM images of B) rGO- Co_3S_4 , C–D) Low and high-magnification TEM images of PANI/rGO- Co_3S_4 . E) CV curves of pure PANI, rGO- Co_3S_4 and PANI/rGO- Co_3S_4 nanocomposites at the scan rate of 100 mV s^{-1} , F) GCD curves of pure PANI, rGO- Co_3S_4 and PANI/rGO- Co_3S_4 nanocomposites at the current density of 1 A g^{-1} and G) Plot of specific capacitance vs current density of PANI/rGO- Co_3S_4 nanocomposite and pure PANI. Reproduced from Ref. [25] with permission. Copyright (2018) Hydrogen Energy Publications LLC.

(Figure 6F) among all other nanocomposites due to the high electrochemically active surface of the electrode material and the synergistic effect between rGO–Co₃S₄ and PANI. In fact, a conductive network is formed between PANI chains and rGO–Co₃S₄ due to the extended π–π interactions. In addition, the PANI/rGO–Co₃S₄ retained 74% of capacitance when the current density was increased from 1 to 20 A g⁻¹ (Figure 6G), in contrast with pure PANI whose capacitance decreased to 69% under similar conditions. The specific capacitance of the PANI/rGO–Co₃S₄ nanocomposite was 767 F g⁻¹ at a current density of 1 A g⁻¹, a reasonably high value. Energy densities as high as 96.9, 88.8, 78.6, 70.1, and 61.2 Wh kg⁻¹ were measured at power densities respectively of 0.5, 1.0, 2.4, 4.5, and 8.8 kW kg⁻¹.

4.2. Monometallic Sulfides as Shell Materials

Similarly, in the materials of previous category, cobalt and nickel are widely used combined with sulfide in shell structures. Besides the hydrothermal deposition and growth, electro-

deposition is a promising method for immobilization of metal sulfides outside or inside nanostructures. Liu and co-workers^[22] used this method for electrodeposition of CoS (shell) on hierarchical MnCo₂O₄ nanostructures (core). MnCo₂O₄ nanowires or nanosheets (MCO-NW@CS or MCO-NS@CS) arrays can be prepared in the absence or presence of ammonium fluoride. The fabrication process of the MCO-NW@CS and MCO-NS@CS nanostructures by hydrothermal and electrodeposition methods is shown in Figure 7A. The individual MCO-NWs are up to several microns long (diameter of ~80 nm, Figure 7B–7C) and generate hierarchical core/shell MCO-NW@CS arrays after electrodeposition of cobalt sulfide (Figure 7D–7E). The ultrathin CoS layers are interconnected with each other and cover uniformly the nanowire surface while preserving the original aligned structure of MCO-NWs, as confirmed by TEM (Figure 7F). In contrast, after incorporation of NH₄F in the first *in-situ* hydrothermal deposition process, the morphology of MnCo₂O₄ changes into about 30 nm thick intercrossed and interconnected nanosheets forming hierarchically intricate and highly porous network arrays (Figure 7G–7H). After CoS electro-

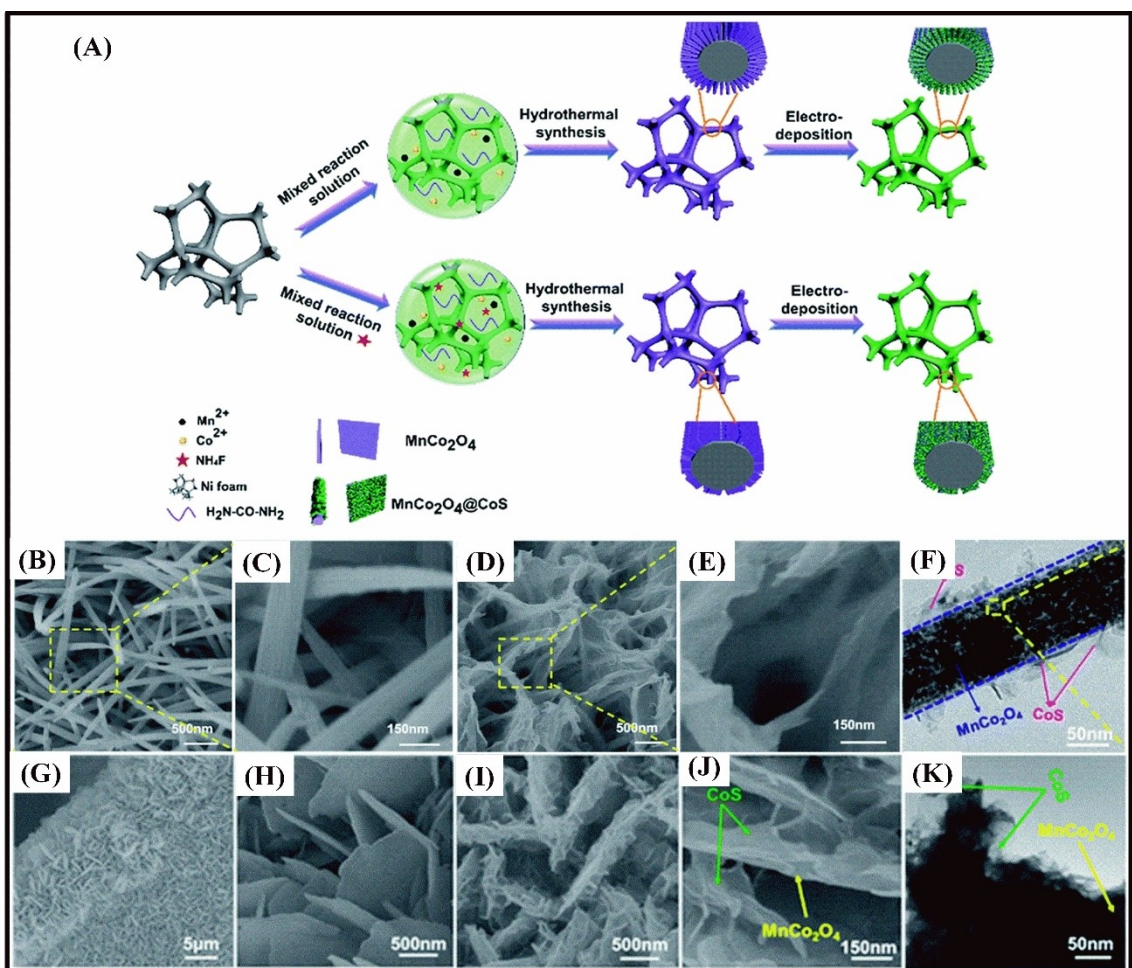


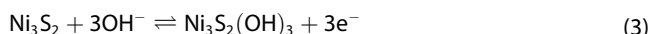
Figure 7. A) Scheme illustrating the core/shell MCO-NW@CS and MCO-NW@NS materials fabrication process. SEM images of the B–C) MnCo₂O₄ and D–E) MnCo₂O₄@CoS nanowire array electrodes at two magnifications; F) TEM image of MCO@CS composite electrode material, G–H) SEM images of the MnCo₂O₄ with nanosheet structure electrode, I–J) SEM images of core/shell MCO-NS@CS arrays electrode at various magnification and K) TEM images of MCO-NS@CS composite electrode. Reproduced from Ref. [22] with permission. Copyright (2017) Royal Society of Chemistry.

deposition (Figure 7I–7J), the MnCo_2O_4 nanoarrays were uniformly coated with a thin nanostructured layer, resulting in thicker hierarchical core/shell MCO-NS@CS arrays (Figure 7K), increasing the electrode/electrolyte contact area and making the access of electrons and ions to the electrode surface much easier, thus improving the energy storage properties of the resultant material.

The synergistic effect of MnCo_2O_4 and CoS promotes the increase of the surface area and consequently improves the charge accumulation and storage. This boosts the electrochemical activity of the interconnected components by making the diffusion of electrons and electrolyte ions blazing faster.

The porous core/shell MCO-NS@CS electrode material exhibits the highest specific capacitance values in relation to the other electrode materials, about 1607.4 F g^{-1} at 0.8 A g^{-1} , a much larger value than of analogous electrodes based on MnCo_2O_4 nanowire arrays (MCO-NW@CS, 1204.6 F g^{-1}). In addition, the supercapacitor prepared with MCO-NS@CS showed a maximum energy density of 55.1 Wh kg^{-1} at the average power density of 477.3 W kg^{-1} , thus corroborating the great potential of MnCo_2O_4 metal oxide nanostructures formed in combination with metal sulfide, as energy storage materials.

Indeed, micro-/nanostructured cobaltites based on ACo_2O_4 ($\text{A}=\text{Ni, Mn, Zn, Cu, Mg, etc.}$) have been widely explored as excellent electrode materials because of their high electrochemical activity, better electrical conductivity, and synergistic effects. MnCo_2O_4 is of special interest due to its high theoretical specific capacitance. Lv and co-workers^[26] used MnCo_2O_4 (core) and Ni_3S_2 (shell) to assemble high-performance supercapacitors. Ni_3S_2 nanosheets were homogeneously synthesized onto hexagonal prism-like MnCo_2O_4 nanocrystals on Ni foam (NF) by the hydrothermal method, followed by calcination. This leads to micro-structured electrodes showing a high specific capacitance of 2807 F g^{-1} at 3 A g^{-1} , as well as superior rate capability (69% capacitance retention at 30 A g^{-1}). The redox reactions of $\text{MnCo}_2\text{O}_4@\text{Ni}_3\text{S}_2$ involved in the energy storage process are [Eqs. (1)–(3)]:



The above half-reactions show that both, MnCo_2O_4 and Ni_3S_2 , contribute simultaneously to the electrochemical reactions thus improving the specific capacitance.

Liu and co-workers^[27] reported an interesting method to enhance the electrochemical activity of MoS_2 . They showed by theoretical and experimental means that the incorporation of phosphorus into MoS_2 yields efficient active sites. It enhances the transfer of Na^+ ions, and improves the intrinsic electrical conductivity, thus improving the kinetics of Na^+ intercalation reaction. The SC device assembled with such electrode material demonstrated a high specific capacitance of 445 F g^{-1} at a current density of 1 A g^{-1} , and energy density of 67.4 Wh kg^{-1} at a power density of 850 W kg^{-1} . Moreover, the device had

considerable cycling stability, exhibiting a capacitance retention of 93.4% after 5000 cycles.

4.3. Monometallic Sulfides as Core and Shell Materials

Materials morphology and structure have significant effects on the properties of supercapacitors. Considering the monometallic sulfides as core and shell materials, their nanowires, nanosheets, hollow nanostructures, and nanoflakes are promising species for fabrication of supercapacitors. Hollow 3D nanostructures can increase the availability of electrochemical reaction sites while shortening the charge transfer distances, thus enhancing the performance of electrode materials. Cheng and co-workers^[28] fabricated a hollow $\text{Ni}_3\text{S}_2/\text{NiS}@\text{Ni}_3\text{S}_4$ nanostructured material based on an one-step hydrothermal method, using the concentration of cetyltrimethyl ammonium bromide (CTAB) to control the size of sub-microspheres (Figure 8A). $\text{Ni}_3\text{S}_2/\text{NiS}$ with higher performance was used as core and Ni_3S_4 nanoflakes with lower performance were used as shell. The combination of high capacitance Ni_3S_4 with high conductivity Ni_3S_2 enhances the charge storage properties of the resultant material.

The size of the core/shell nanosphere was controlled by adjusting the concentration of CTAB to 21.5, 43.0, and 64.5 mmol L^{-1} producing 504, 306 and 233 nm diameter nano-hollow spheres (Figure 8B–8D), respectively labeled as NHS-0, NHS-1, and NHS-2. The XRD patterns demonstrated that all nickel sulfide phases (Ni_3S_2 , NiS and Ni_3S_4) are present in those materials, but the best performance was achieved when the concentration of CTAB was 64.5 mmol L^{-1} . This behavior was assigned to the cage and the Kirkendall effects, and to the Ostwald ripening mechanism. Indeed in a concentration higher than the critical micelle concentration, the CTAB molecules assembled into micelles and closed bilayer aggregates work as plenteous cages that break down the continuous aqueous solution into a myriad of small regions.^[28]

The NHS-3, owning the smallest diameter, exhibits the highest specific capacity of 1031.3 C g^{-1} (286.5 mAh g^{-1}) at the current densities of 2 A g^{-1} , whereas NHS-1 (830.0 C g^{-1} , 230.5 mAh g^{-1}) and NHS-2 (855.8 C g^{-1} , 237.7 mAh g^{-1}) presented similar but much lower capacity values. This result proves that the control of morphology is fundamental to achieve a good electrochemical performance. In fact, the electrochemical impedance spectra (EIS) showed that the equivalent series resistance (R_{ESR}) and charge-transfer resistance (R_{ct}) of NHS-3 were much smaller than that of Ni_3S_4 , and the diameter of the corresponding arc in IES can be almost negligible. In other words, the charges can move more easily from the electrolyte to the electrode side in the NHS-3 electrode.^[28] This feature and synergistic effects associated with the interconnected nickel sulfide three phases resulted in the high specific and energy density of 37.7 Wh kg^{-1} at the power density of 801 W kg^{-1} .

Shi *et al.*^[29] fabricated nanowire arrays made of $\text{Ni}_3\text{S}_2/\text{MoS}_2$ deposited on nickel foam by a hydrothermal process. In fact, the nanostructured material was made of a Ni_3S_2 core and

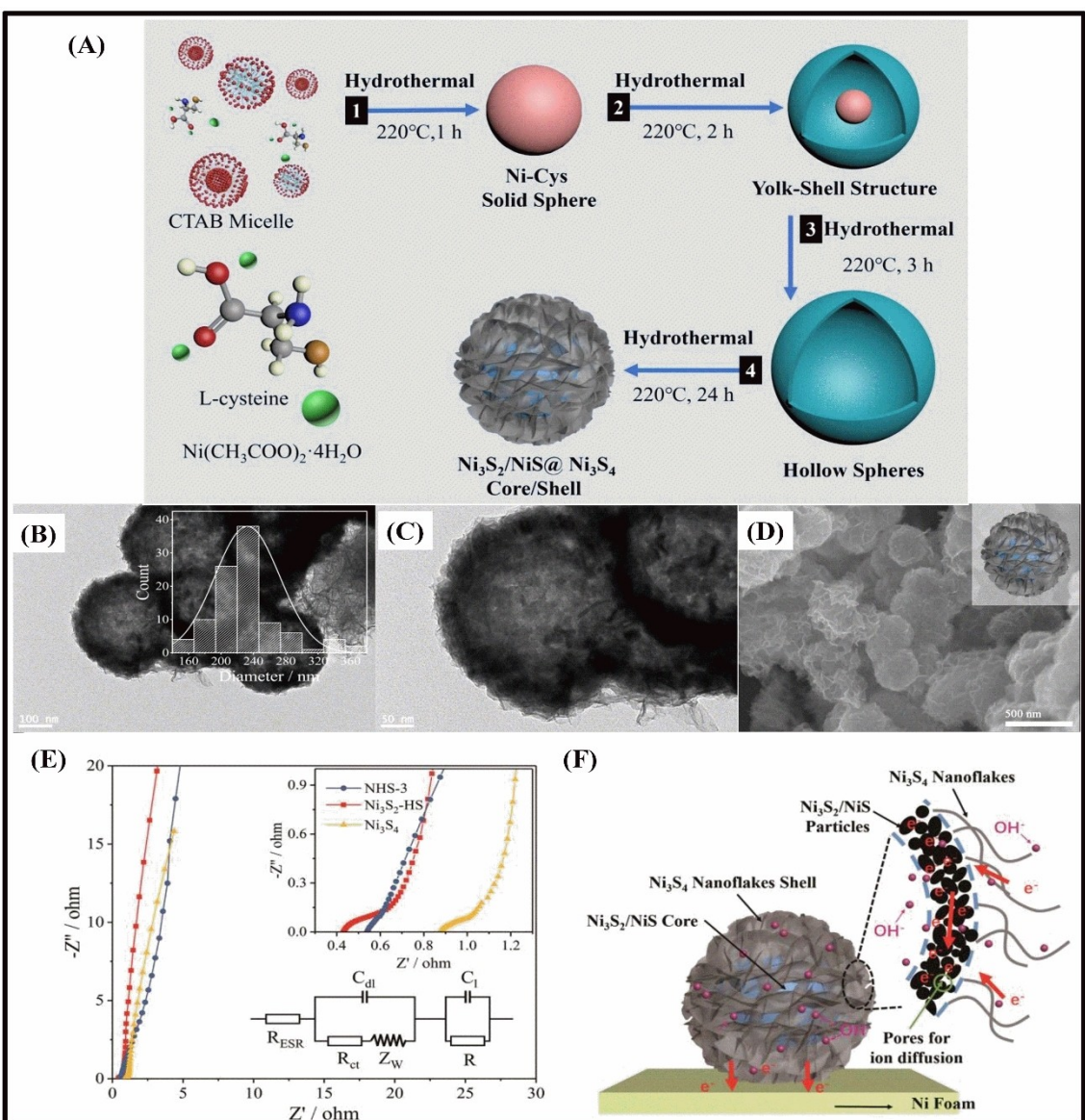


Figure 8. A) Scheme showing the fabrication process of the $\text{Ni}_3\text{S}_2/\text{NiS@Ni}_3\text{S}_4$ hollow sub-microspheres, B–C) TEM and D) respective SEM image. E) Nyquist plots of NHS-3, Ni_3S_2 -HS and Ni_3S_4 electrodes, and the expanded high-frequency region, as well as the corresponding equivalent circuit are shown in the inset. F) The schematic of the hybrid $\text{Ni}_3\text{S}_2/\text{NiS@Ni}_3\text{S}_4$ nanostructured material. Reproduced from Ref. [28] with permission. Copyright (2018) Elsevier Ltd.

$\text{Ni}_3\text{S}_2/\text{MoS}_2$ nanosheet shell to enhance the specific capacity. The SC device made of electrodes with a mass loading of 6.3 mg cm^{-2} showed a significant specific capacitance (8.04 F cm^{-2}), cycling stability, and energy density of $718.88 \mu\text{Wh cm}^{-2}$ at a power density of 8.5 mW cm^{-2} , due to the unique morphologic and electronic properties of that material. Liu *et al.* fabricated a flexible device by using a family of metal sulfides ($\text{Co}_9\text{S}_8-\text{MoS}_2$, $\text{Co}_9\text{S}_8-\text{NiS}_2$, $\text{Co}_9\text{S}_8-\text{NiCo}_2\text{S}_4$, $\text{NiCo}_2\text{S}_4-\text{CuS}$, $\text{NiCo}_2\text{S}_4-\text{NiS}_2$, and $\text{NiCo}_2\text{S}_4-\text{MoS}_2$) deposited on carbon cloth.^[30] In their study, the best result was obtained when they used mixed metal sulfides instead of a single metal sulfide electrode material such as Co_9S_8 . For example, the device made of $\text{Co}_9\text{S}_8-\text{NiCo}_2\text{S}_4$ showed a specific capacity of $337.78 \text{ mAh g}^{-1}$ at a current density of 1 A g^{-1} , and a potential window of -1 to 1.6 V . Jiang's group devised a porous

$\text{Co}_3\text{S}_4@\text{Ni}_3\text{S}_4$ heterostructure array material with vertical channels for electron and ion diffusion.^[31] In their work Co_3S_4 worked as core and Ni_3S_4 as shell which enhanced the charge and ion transfer, resulting in an areal capacitance (C_A) of 3.6 F cm^{-2} at 0.8 mA cm^{-2} , energy densities of 0.19 – $0.021 \text{ mWh cm}^{-2}$ in the power density range of 1.72 to 38.4 mW cm^{-2} , while preserving 80% of the initial C_A even after 5000 charge-discharge cycles. A summary of the above reports with more information about the device properties is presented in Table 1.

5. Bimetallic Sulfide Core@Shell Structures

In recent years, the bimetallic sulfides have produced great interest in the scientific community, because of their high

Table 1. Comparison of the relevant electrochemical parameters of transition metal sulfide-based core@shell materials and their performance in SC type energy storage devices assembled with a suitable cathode material.^[a]

Materials	Specific capacitance [F g^{-1}]	Specific capacity [C g^{-1}]	Potential window	Rate capability [A g^{-1}] (retention [%])	Cycles (stability retention [%])	Highest energy density: [Wh kg^{-1}]	Highest power density [W kg^{-1}]	Negative electrode material	Synthesis methods Core Shell	Ref.
Core	$\text{mSiO}_2@\text{Ni}_3\text{S}_2/\text{NiS}_2$	449.7 at 1 A g^{-1}	80946 at 1 A g^{-1}	-0.5– ~1.3 V	1–20 (~18)	8,000 (200)	41.67	5584.95	$\text{mSiO}_2@\text{Ni}_3\text{S}_2/\text{NiS}_2$	HT HT [23]
Shell	PANI/ $\text{rGO}-\text{C}_{93}\text{S}_4$	767 at 1 A g^{-1}	767 at 1 A g^{-1}	-0.2–0.8 V vs. SCE (74)	1–20	5,000 (81.7)	96.9	8800	—	HT PL [25]
	MCO-Ni@CoS	1607.4 at 0.8 A g^{-1}	723.3 at 0.8 A g^{-1}	0.0–0.45 V vs. Ag/ (–)	0.8–16	5000 (91.5)	55.1	12380	AC	HT ED [22]
MCO-NW@CS	1204.6 at 0.8 A g^{-1}	542.1 at 0.8 A g^{-1}	—	0.0–0.45 V vs. Ag/ (–)	0.8–16	5000 (90.1)	—	—	—	HT ED [22]
Core and shell	$\text{MnCo}_2\text{O}_4@\text{Ni}_3\text{S}_2$	2807 at 3 A g^{-1}	1122.8 at 3 A g^{-1}	0.0–0.4 V vs. SCE (69)	3–30	5,000 (92)	—	—	—	HT HT [26]
	CSHs $\text{Ni}_3\text{S}_2/\text{NiS}@\text{Ni}_3\text{S}_4$	1875 at 2 A g^{-1}	1031.3 at 2 A g^{-1}	0.0–0.55 V vs. Hg/ (59.6)	2–40	3,000 (90.3)	37.7	801	rGO	HT HT [28]
	$\text{Ni}_3\text{S}_2/\text{MoS}_2$	8.04 F cm^{-2} at 2 mA cm^{-2}	5.63 F cm^{-2} at 2 mA cm^{-2}	-0.2– 0.5 $\text{V}^{\text{b}[\text{b}]}$	2–15 mA cm^{-2} (87.1)	3,000 (76)	718.88 $\mu\text{Wh cm}^{-2}$	42.5 0.19 38.4 mWh cm^{-2}	AC	HT HT [29]
<hr/>										
[a] SCE: saturated calomel electrode, HT: hydrothermal, ED: electrodeposition, CSHs: core-shell heterostructures. [b] Reference electrode information not available.										

electrical conductivity, large capacitance and excellent thermal stability.^[10–11] Another additional great advantage of those materials as compared to monometallic sulfides is the possibility of modulating its properties by adjusting the ratio of the metallic components. In fact, compared to monometallic sulfides, the bimetallic ones have more constituents with rich valence states resulting in multifarious redox reactions.^[32]

Despite the excellent properties mentioned above, the bimetallic sulfides still have a limited specific capacitance and a short life cycle due to the presence of fast parallel reactions, which restrict their practical application in energy storage devices.^[33] However, in order to improve the specific capacitance and life cycle of bimetallic sulfides, hierarchical 3D core@shell structures have been designed, where the core and shell materials should have respectively high electrical conductivity and high specific capacitance.^[34] Interestingly, bimetallic sulfides have such features and it can be used either as core or as shell or even both.

The most relevant works reported in the literature between the years 2017 and 2020 using bimetallic sulfides in core@shell structures as electrode material are listed in Table 2.

5.1. Bimetallic Sulfides as Core Materials

As mentioned previously, most of bimetallic sulfides used as core in core@shell structures are Ni and Co spinels where the nickel and cobalt ions occupy tetrahedral and octahedral sites, respectively. Also, most of the shell materials in the bimetallic core@shell structures with metal sulfide core are metal oxides, as can be seen in Table 2.

The bimetallic sulfide cores have been synthesized by hydrothermal method in several shapes such as nanowires, nanosheets, nanotubes, among others.^[35,42–43,59] Generally, those nanostructures are grown on substrates like nickel foam (NF) and carbon cloth (CC), since they act as a high surface area conducting skeleton to support the bimetallic sulfide core structure. In fact, Zhao and co-authors^[35] obtained NiCo_2S_4 nanowires on CC substrate using hydrothermal method. After obtaining the NiCo precursor on CC substrate, the modified substrate was immersed into a Na_2S solution and kept at 120 °C for 6 hours. The as prepared NiCo_2S_4 nanowires/CC was immersed in a solution of $\text{Co}(\text{NO}_3)_3 \cdot 6\text{H}_2\text{O}$ and $\text{Na}_2\text{MoO}_4 \cdot 2\text{H}_2\text{O}$ and the mixture heated at 160 °C for 6 hours. After that, the sample was annealed at 300 °C for 2 hours under Ar atmosphere, to get the $\text{NiCo}_2\text{S}_4 @ \text{CoMoO}_4$ core@shell material, as shown in Figure 9A. TEM images revealed that the NiCo_2S_4 core presents a porous structure and the CoMoO_4 nanosheets are anchored on the surface forming the shell (Figure 9B).

The $\text{NiCo}_2\text{S}_4 @ \text{CoMoO}_4$ electrode presented a specific capacitance of 2118.8 F g^{-1} at 1 A g^{-1} , and its electrochemical behavior proved to be much superior compared to its isolated components. Indeed, the rate capability of $\text{NiCo}_2\text{S}_4 @ \text{CoMoO}_4$ was 81.6% at 20 A g^{-1} , while of NiCo_2S_4 and CoMoO_4 was 73.9% and 79%, respectively. Even after 5,000 galvanostatic charge-discharge cycles, the $\text{NiCo}_2\text{S}_4 @ \text{CoMoO}_4$ electrode exhibited a retention capacity of 88.6%. Also, the authors build an asymmetric supercapacitor device using activated carbon (AC) as the negative electrode which delivered a high energy density of 66.6 Wh kg^{-1} and a maximum power density of 16 kW kg^{-1} . Such properties were assigned to the high specific capacitance and good conductivity of NiCo_2S_4 nanowires that provide higher density of electron transport channels, improv-

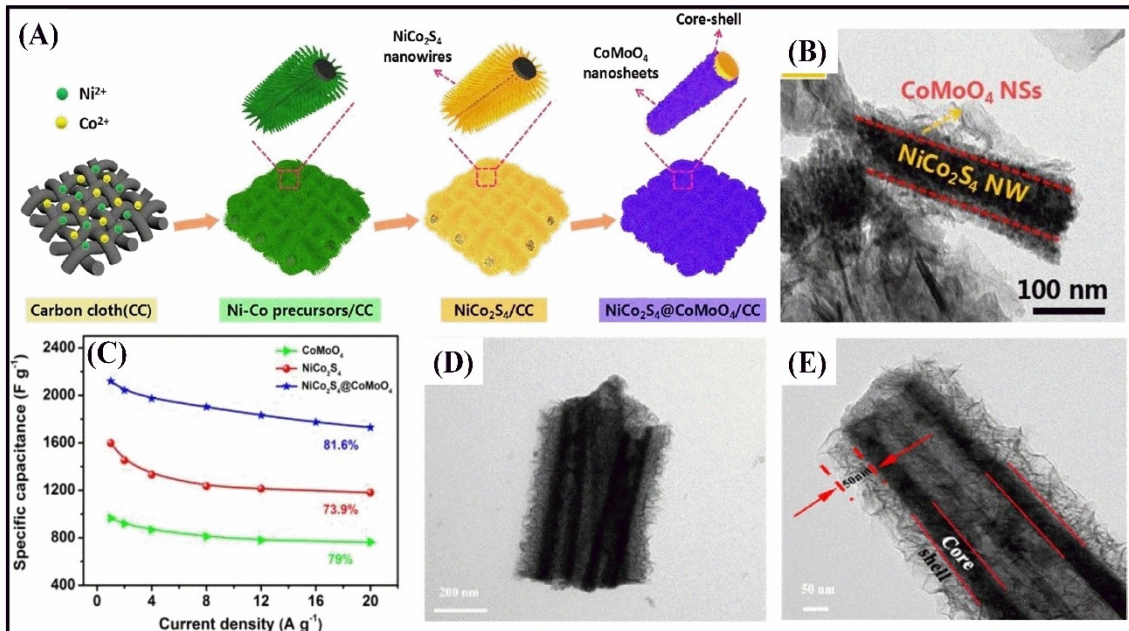


Figure 9. Schematic illustration of $\text{NiCo}_2\text{S}_4 @ \text{CoMoO}_4$ core@shell material preparation steps (A). TEM image of $\text{NiCo}_2\text{S}_4 @ \text{CoMoO}_4$ (B) and specific capacitance of CoMoO_4 , NiCo_2S_4 and $\text{NiCo}_2\text{S}_4 @ \text{CoMoO}_4$ as a function of the current density. Reproduced from Ref. [35] with permission. Copyright (2018) Published by Elsevier B.V. TEM and HRTEM images of $\text{FeCo}_2\text{O}_4 @ \text{Ni(OH)}_2$ (D and E). Reproduced from Ref. [45] with permission. Copyright (2020) Published by Elsevier Ltd.

Table 2. Comparison of the relevant electrochemical parameters of bimetallic sulfide core@shell-based materials and their performance in SC type energy storage devices assembled with a suitable cathode material.^[a]

Materials	Specific capacitance [Fg^{-1}]	Specific capacity [Cg^{-1}]	Potential window	Rate capability [Ag^{-1}] (retention [%])	Cycles (stability retention [%])	Highest energy density [Whkg^{-1}]	Highest power density [Wkg^{-1}]	Negative electrode material	Synthesis methods	Ref.
Core	NiCo ₂ S ₄ @CoMoO ₄ NiCo ₂ S ₄ @NiCo ₂ O ₄ NiCo ₂ S ₄ @NiCo ₂ O ₄	2118.8 2258.9 1590	10594 Cg ⁻¹ at 1 Ag ⁻¹ 10165 Cg ⁻¹ at 5 Ag ⁻¹ 874.5 Cg ⁻¹ at 5 Ag ⁻¹	0.0–0.5 V vs. SCE 0.0–0.45 V vs. SCE –0.1– +0.45 V vs. Ag/AgCl	1–20 (81.6) 0.5–12.5 (50.4)	5,000 (88.6)	66.6	16,000	AC	HT HT [35]
	NiCo ₂ S ₄ @NiMoO ₄ ·xH ₂ O NiCo ₂ S ₄ @Ni(OH) ₂	830.2 –	415.1 Cg ⁻¹ at 2 Ag ⁻¹ 404.2 mAcm ⁻² at 2 Ag ⁻¹ or 1455.1 Cg ⁻¹	0.0–0.5 V vs. Hg/HgO 0.0–0.5 V vs. Hg/HgO	1–20 (45.9) 2–50 (26.12)	2,000 (96)	32	375	rGO	HT HT [36]
	NiCo ₂ S ₄ @NiCoP NiCo ₂ S ₄ @PPANI	5.98 Fcm ⁻² 4.74 Fcm ⁻²	2.99 Ccm ⁻² at 1 mAcm ⁻² 2.84 Ccm ⁻² at 2 mAcm ⁻² 2.56 Fcm ⁻² at 1 mAcm ⁻²	0.0–0.5 V vs. Hg/HgO 0.0–0.6 V vs. Hg/HgO	1–50 mAcm ⁻² (70.3) 2–50 mAcm ⁻² (73.8)	5,000 (92.9)	0.135 mWhcm ²	0.755 mWhcm ²	AC	HT HT [40]
	CuCo ₂ S ₄ @CoMoO ₄ CuCo ₂ S ₄ @NiCoAl-LDH	5.56 Fcm ⁻² 1876	2.22 Ccm ⁻² at 1 mAcm ⁻² 938 g ⁻¹	0.0–0.4 V vs. [b] 0.0–0.5 V vs. SCE	1–22 mAcm ⁻² (~7)	30,000 (108)	64.92	276.23	graphene	HT ED [41]
	CuCo ₂ S ₄ @Ni ₂ (CO ₃)(OH) ₂ FeCo ₂ S ₄ @Ni(OH) ₂	5.16 Fcm ⁻² –	2.58 Ccm ⁻² at 2 mAcm ⁻² 239.72 mAhhg ⁻¹ at 1 Ag ⁻¹ or 863 Cg ⁻¹	0.0–0.5 V vs. SCE 0.0–0.34 V vs. Ag/AgCl	2–50 mAcm ⁻² (~40) 1–8	10,000 (95.74)	45.73	198.8	AC	HT HT [42]
	Zn _{0.76} Co _{0.24} S ₂ @Ni ₃ S ₂ Co ₃ O ₄ @CoNi ₂ S ₄	–	1209 Cg ⁻¹ at 2 Ag ⁻¹ 244.4 at 1 Ag ⁻¹ or 879.8 Cg ⁻¹	0.0–0.5 V vs. SCE 0.0–0.45 V vs. Ag/AgCl	2–20 (78.6) 1–16 (81.3)	5,000 cycles (94.5)	53.8 at 853 W kg ⁻¹	~9000 at ~35 Whkg ⁻¹	AC	HT and SP ED [43]
Shell	CuCo ₂ O ₄ /CuO@NiCo ₂ S ₄	10.33 Fcm ⁻² at 10 mAcm ⁻²	4.24 Ccm ⁻² at 10 mAcm ⁻²	0.0–0.4 V vs. Hg/HgO	5–20 mAcm ⁻² (83.2)	10,000 (93.2)	0.824 mWhcm ⁻²	8 mWcm ⁻²	AC	HT ED [44]
	CuO/Cu ₂ O@NiCo ₂ S ₄	3.186 Fcm ⁻² at 10 mAcm ⁻²	1.27 Ccm ⁻² at 10 mAcm ⁻²	0.0–0.4 V vs. Ag/AgCl	2–50 mAcm ⁻² (82.06)	2,000 (96.73)	–	–	–	Thermal ED [45]
	MWCNT/NiCo ₂ S ₄ PNTs@NiCo ₂ S ₄	1423.7 911	569.5 Cg ⁻¹ at 2.5 Ag ⁻¹ 455.5 Cg ⁻¹ at 1 Ag ⁻¹	0.0–0.4 V vs. Ag/AgCl 0.0–0.5 V vs. SCE	2.5–25 (70.9) 1–20 (65.0)	4,000 (81.4)	37.2	1425.53	MWCNT/ NiCo ₂ S ₄ PNTs@NiCo ₂ S ₄	CVD HT [50]
	Cu@Ni@NiCoS	–	6.94 μAhcm ²	0.0–0.45 V vs. SCE	0.04–0.5 mAcm ² (78.7)	10,000 (89)	0.48 μWhcm ²	11.15 μWhcm ²	Cu@Ni@NiCoS	Soft-template ES HT Anion ex-change ED [51]
	MnCo ₂ O ₄ @MnCo ₂ S ₄ Co ₃ S ₄ @FeCo ₂ S ₄	1933.33 2695	773.33 Cg ⁻¹ 1078 Cg ⁻¹ at 1 Ag ⁻¹	0.0–0.4 V vs. Ag/AgCl	1–10 (68.9) 1–10 (69.8)	– 1,000 (84)	50.75 43.6 at 770 W kg ⁻¹	1260 5510 at 13.3 Whkg ⁻¹	CNTs rGO IE	Anion ex-change HT ED [52]
Core and shell	CoMoS ₄ @Ni-Co-S MnCo ₂ S ₄ @Ni-Co-S	2208.5 10.14 F cm ⁻²	883.4 Cg ⁻¹ – at 1 mAcm ⁻²	0.0–0.4 V vs. Ag/AgCl 0.0–0.4 V vs. Ag/AgCl	1–20 (68.8) 2–50 (82.3)	5,000 (91.3) 5,000 (62.7)	49.1 7.26 Whm ⁻²	800 30.5	AC	HT ED [53]

Materials	Specific capacitance [F g ⁻¹]	Specific capacity [C g ⁻¹]	Potential window	Rate capability [A g ⁻¹] (retention [%])	Cycles (stability retention [%])	Highest energy density [Wh kg ⁻¹]	Highest power density [W kg ⁻¹]	Negative electrode material	Synthesis methods	Core	Shell	Ref.
ZnCo ₂ S ₄	10.14 F cm ⁻² at 1 mA cm ⁻²	4.01 C cm ⁻² at 1 mA cm ⁻²	0.0–0.45 V vs. Hg/HgO	2–15 (54.8)	5,000 (95.5)	51.7	1700	AC	SOV	SOV	[57]	
CoNi ₂ S ₄	2035 at 1 A g ⁻¹	814 C g ⁻¹	0.0–0.4 V vs. SCE	1–20 (59.7)	3,000 (91.3)	25.2	110	–	HT	HT	[33b]	
CuCo ₂ S ₄ @NiCo ₂ S ₄	–	537.12 C g ⁻¹ at 1 A g ⁻¹	0.0–0.4 V vs. SCE	1–8 (74.5)	5000 (100)	23.4 at 400 W kg ⁻¹	4000 at 400 W kg ⁻¹	AC	HT	HT	[58]	

[a] HT: hydrothermal, ED: electrodeposition, ES: electrospinning, SOV: solothermal. [b] Reference electrode not available.

ing the total capacitance of the core@shell material, as well as to the porous CoMoO₄ nanosheets anchored on the surface of NiCo₂S₄ nanowires that provide short ion transport pathways, facilitating the accessibility of the electrolyte.

In addition to metal oxides, other compounds have been used as shell materials in hierarchical 3D core@shell structure materials. In fact, She *et al.*^[39] developed a NiCo₂S₄@Ni(OH)₂ exhibiting a high specific capacity of 404.2 mAh g⁻¹ at 2 A g⁻¹. However, the rate capability was very poor (26.12%) in the 2 to 50 A g⁻¹ range. Liu and co-authors^[41] coated NiCo₂S₄ nanowires on carbon fibers with polyaniline (PANI) to overcome such a drawback. The combination of PANI with NiCo₂S₄ resulted in a material with high specific capacitance (4.74 F cm⁻² at 2 mA cm⁻²) and a good rate capability (73.8% at 50 mA cm⁻²), as well as excellent capacitance retention (82.6% after 5,000 cycles). Those results show that the combination of PANI with NiCo₂S₄ provides more accessible electroactive sites and high rates of electron diffusion from shell to core.

Other bimetallic sulfides such as CuCo₂S₄, FeCo₂S₄, and CoFe₂S₄ have been used as core materials.^[42–43,45,59] Mao *et al.*^[42] obtained a CuCo₂S₄@CoMoO₄ material on NF substrate using a hydrothermal method followed by a calcination process. Although the specific capacitance of CuCo₂S₄@CoMoO₄ electrode material (5.56 F cm⁻²) at 1 mA cm⁻² was higher than of CuCo₂S₄ (3.71 F cm⁻²) and CoMoO₄ (0.33 F cm⁻²), the rate capability of the CuCo₂S₄@CoMoO₄ electrode was only 5.9% at 22 mA cm⁻².

An interesting strategy was used by Zhou *et al.*^[45] to relieve the expansion of the bimetallic sulfides during the redox process and achieve a superior electrochemical performance. Furthermore, hollow nanotubes based on FeCo₂S₄ core (Figure 9D and 9E) were prepared by controlling the experimental conditions of a two steps hydrothermal synthesis. The FeCo₂(C₂O₄)₃ precursor was prepared in the first step and then the C₂O₄²⁻ anion exchanged by S²⁻ using a Na₂S solution. According to Zhu *et al.*^[60] the fine control on the concentration of S²⁻ and the vulcanization time are fundamental to get the desired hollow nanotubes. Then, Ni(OH)₂ nanosheets were electrodeposited on the FeCo₂S₄ hollow nanotubes, as shown in Figure 9E. The FeCo₂S₄@Ni(OH)₂ electrode presented a specific capacity of 239.72 mAh g⁻¹ at 1 A g⁻¹ and a rate capability of 53.4% at 8 A g⁻¹. The asymmetric supercapacitor assembled with FeCo₂S₄@Ni(OH)₂ as positive electrode and AC as negative electrode delivered an energy density of 55.33 Wh kg⁻¹ at a power density of 800 W kg⁻¹. This superior electrochemical performance is consistent with the higher density of redox sites and faster electron transport and ion transport channels provided by the hollow tubular FeCo₂S₄ and Ni(OH)₂ plates, as well as the relief of tension during the redox reactions and volume expansion of the material.

Lv *et al.*^[46] designed and synthesized hierarchical Zn_{0.76}Co_{0.24}S@Ni₃S₂ core@shell nanosheet arrays on NF, with a bimetallic sulfide-based shell interconnected with numerous vertically aligned Zn_{0.76}Co_{0.24}S nanosheet arrays as core. They are initially prepared by a hydrothermal reaction combined with a sulfurization process and, subsequently, uniformly wrapped with interconnected Ni₃S₂ nanosheet arrays shell

using an electrochemical deposition reaction (Figure 10A). Figures 10B–10C present the typical SEM images of $Zn_{0.76}Co_{0.24}S$ nanosheet arrays, while the $Zn_{0.76}Co_{0.24}S@Ni_3S_2$ core@shell nanosheet arrays exhibiting its integrated architecture are depicted in Figures 10D–10E. The TEM images of $Zn_{0.76}Co_{0.24}S@Ni_3S_2$ is shown in Figures 10F–10G confirming its core@shell structure with a shell made of ultrathin nanosheet arrays.

The $Zn_{0.76}Co_{0.24}S@Ni_3S_2/NF$ electrode achieved a specific capacity of 1209 Cg^{-1} at 2 Ag^{-1} and 78.6% of this value at 20 Ag^{-1} , which is respectively 2.5 and 3.4 times larger than the specific capacitance of the isolated sulfides, $Zn_{0.76}Co_{0.24}S/NF$ (476 Cg^{-1} at 2 Ag^{-1} , 63.9% rate capability at 20 Ag^{-1}) and Ni_3S_2/NF electrodes (360 Cg^{-1} at 2 Ag^{-1} , 57.5% rate capability at 20 Ag^{-1}). Furthermore, exhibited a capacity retention of 94.9% after 5000 cycles, against 86.5% and 83.1% respectively of $Zn_{0.76}Co_{0.24}S/NF$ and Ni_3S_2/NF electrodes. In addition, the fabricated $Zn_{0.76}Co_{0.24}S@Ni_3S_2/NF//AC$ asymmetric solid-state supercapacitor delivered the maximum energy density of 53.8 Wh kg^{-1} at 853 W kg^{-1} and the maximum power density of 9000 W kg^{-1} at 35 Wh kg^{-1} , specific capacity of 228 Cg^{-1} at 1 Ag^{-1} , with 62.7% rate capability at 10 Ag^{-1} , while retaining 90.3% of its initial capacity and 88.4% of faradic efficiency after 5000 cycles.^[46]

The superior electrochemical performance of this novel composite material was believed to result mainly from the unique integrated architecture in which both the core and shell were composed of interconnected nanosheets. Both have enhanced electrochemical activity, as consequence of the high specific surface area, density of active sites and electric conductivity, with shortened charge transportation pathways,

while providing full contact of the electrode with the electrolyte, thus maximizing the availability of the electroactive sites while hastening the charge-transfer at the electrode/electrolyte interface. Additionally, the Ni_3S_2 nanosheet arrays shell appeared to protect the $Zn_{0.76}Co_{0.24}S$ nanosheet arrays core from agglomeration, alongside having higher electrical conductivity and contributing to immobilize and stabilize the nanosheet shell, thus promoting robust mechanical and electrochemical stability that preserved the integrated architectures during the charge/discharge processes.

5.2. Bimetallic Sulfides as Shell Materials

In the previous section, the bimetallic sulfides prepared by hydrothermal method were explored as core materials, but electrodeposition is the technique of choice when it comes to preparing shell materials based on bimetallic sulfides. In addition to being a simple technique, it is possible to control the amount of material deposited on, especially as high surface area nanosheets, simply by controlling the amount of charge employed.

Zhou *et al.*^[49] prepared a hierarchical copper oxide@ternary nickel cobalt sulfide ($CuO/Cu_2O@NiCo_2S_4$) core@shell electrode material, by first generating the core material (CuO/Cu_2O) by thermal oxidation of a Cu foam, and then proceeding to the electrodeposition of nickel cobalt sulfide ($NiCo_2S_4$) nanosheets on the CuO/Cu_2O nanowires surface. TEM images revealed $NiCo_2S_4$ nanosheets with an average thickness of $\sim 20 \text{ nm}$, and $\sim 50 \text{ nm}$ diameter CuO/Cu_2O NWs. The electrochemical proper-

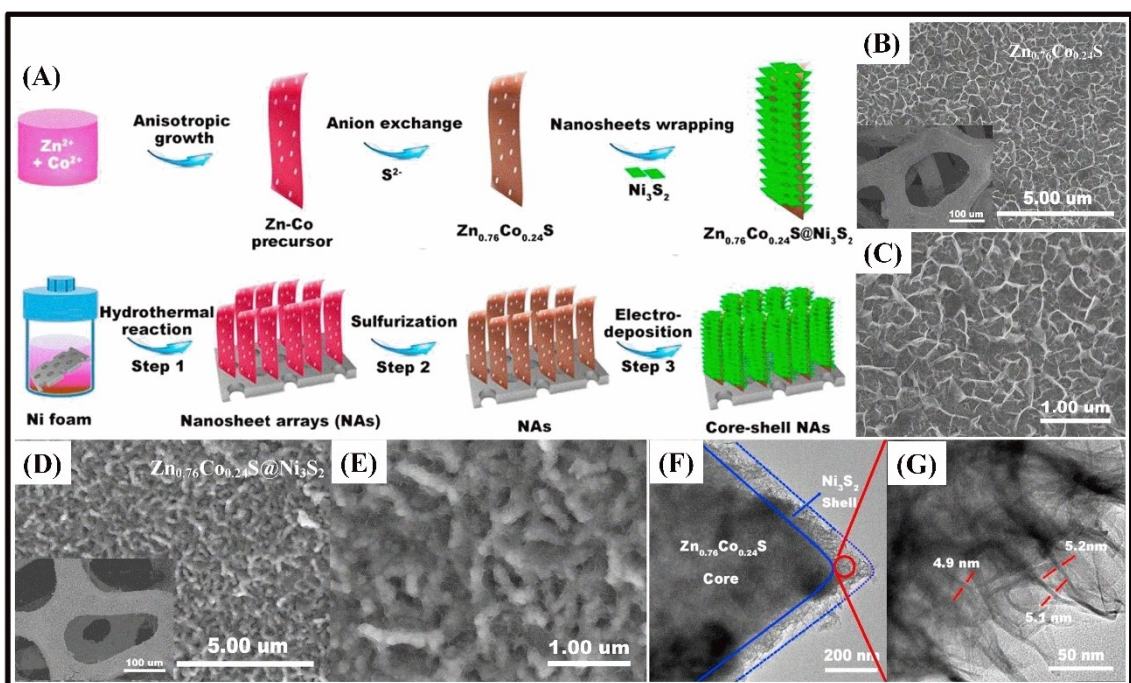


Figure 10. A) Schematic illustration of the synthesis of $Zn_{0.76}Co_{0.24}S@Ni_3S_2$ nanosheet arrays on Ni foam by a stepwise fabrication procedure. B) Typical SEM images of $Zn_{0.76}Co_{0.24}S$ nanosheet arrays and C–E) $Zn_{0.76}Co_{0.24}S@Ni_3S_2$ core@shell nanosheet arrays. F–G) TEM images of $Zn_{0.76}Co_{0.24}S@Ni_3S_2$ core@shell nanosheet arrays. Reproduced from Ref. [46] with permission. Copyright (2018) Elsevier B.V.

ties of CuO/Cu₂O@NiCo₂S₄ were evaluated and a specific capacitance of 3.158 F cm⁻² at 10 mA cm⁻² was demonstrated, as well as an excellent rate capability of 82.06% from 2 to 50 mA cm⁻².

Similarly, Zhang *et al.*^[48] electrodeposited NiCo₂S₄ nanosheets on CuCo₂O₄/CuO nanocomposite in order to obtain a hierarchical 3D core@shell material. As shown in Figure 11A, the CuCo₂O₄ core has a nanoporous structure and ~100 nm diameter, whereas the ~80 nm thick NiCo₂S₄ nanosheets are coating the CuCo₂O₄/CuO surface in CuCo₂O₄/CuO@NiCo₂S₄ (Figure 11B). The electrode made of this material achieved an ultrahigh specific capacitance of 10.33 F cm⁻² at 10 mA cm⁻², as well as a good rate capability of 83.2% from 5 to 20 mA cm⁻². Even after 10,000 galvanostatic charge-discharge cycles, the CuCo₂O₄/CuO@NiCo₂S₄ electrode showed a charge retention of 93.2% (Figure 11C). In addition, the asymmetric supercapacitor assembled with it as positive and AC as negative electrode, respectively, presented an energy density of 0.824 mWh cm⁻² at a power density of 8 mW cm⁻², with a charge retention of 91.2% after 10,000 cycles at 20 mA cm⁻².

Multiwall carbon nanotubes (MWCNT) and polypyrrole have also been combined with bimetallic sulfides in order to obtain hierarchical 3D core@shell structures. In fact, Beka *et al.*^[50] grew MWCNT by CVD process, then deposited a Ni–Co precursor on MWCNT using a hydrothermal method, and the obtained MWCNTs-NiCo was hydrothermally processed in a sulfide solution to get MWCNT@NiCo₂S₄. The electrochemical performance of MWCNT@NiCo₂S₄ was evaluated demonstrating a specific capacitance of 1423.7 F g⁻¹ at 2.5 A g⁻¹, and a good rate capability of 70.9% from 2.5 to 25 A g⁻¹. Zhang *et al.*^[51] reported

a core@shell material based on polypyrrole nanotubes (PNTs) as core and NiCo₂S₄ as shell. The TEM image displayed in Figure 11D shows NiCo₂S₄ nanosheets composed by nanoparticles subunits anchored on PNTs surface.

The PNTs@NiCo₂S₄ electrode presented an electrochemical behavior superior to pure NiCo₂S₄ and PNTs electrodes, as can be seen in Figure 11. Indeed, it presented a current intensity twice as large and almost six times higher than NiCo₂S₄ and PNTs electrodes, respectively. In consequence, the specific capacitance of PNTs@NiCo₂S₄ (911 F g⁻¹) was much larger than of NiCo₂S₄ (470 F g⁻¹) and PNTs (125 F g⁻¹) alone at 1 A g⁻¹. The capacitance retention of PNTs@NiCo₂S₄, NiCo₂S₄, and PNTs from 1 to 20 A g⁻¹ was respectively 64.9%, 44.7% and 46.4%. In addition, the symmetric SC assembled with PNTs@NiCo₂S₄, NiCo₂S₄, and PNTs from 1 to 20 A g⁻¹ was respectively 64.9%, 44.7% and 46.4%. In addition, the symmetric SC assembled with PNTs@NiCo₂S₄ as positive and negative electrodes presented a high energy density of 21.3 Wh kg⁻¹ at 417 W kg⁻¹ and power density as high as 8.6 kW kg⁻¹ at 11.3 Wh kg⁻¹.

Le *et al.*^[54] prepared on NF hierarchical hollow Co₃S₄@FeCo₂S₄ nanostructures with a bimetallic sulfide-based shell, according to the method schematized in Figure 12A. Firstly, 2D Co-MOF nanoarrays were assembled on NF (Co-MOF/NF) via a simple solution reaction (Figure 12B), FeCo-LDHs nanosheets were prepared on the surface of etched Co-MOF nanoarrays (Figure 12C) by on-exchange/etching process, and finally converted into intersected FeCo₂S₄ nanosheets assembled on the surface of Co₃S₄ hollow nanoarrays (Figure 12D) by a hydrothermal sulfurization method. The Co₃S₄@FeCo₂S₄ electrode exhibited a specific capacitance of 2695 F g⁻¹ at 1 A g⁻¹, retaining 69.8% of its capacitance at 10 A g⁻¹ and 84% of the capacity after 1000 cycles. On the other hand, the Co₃S₄

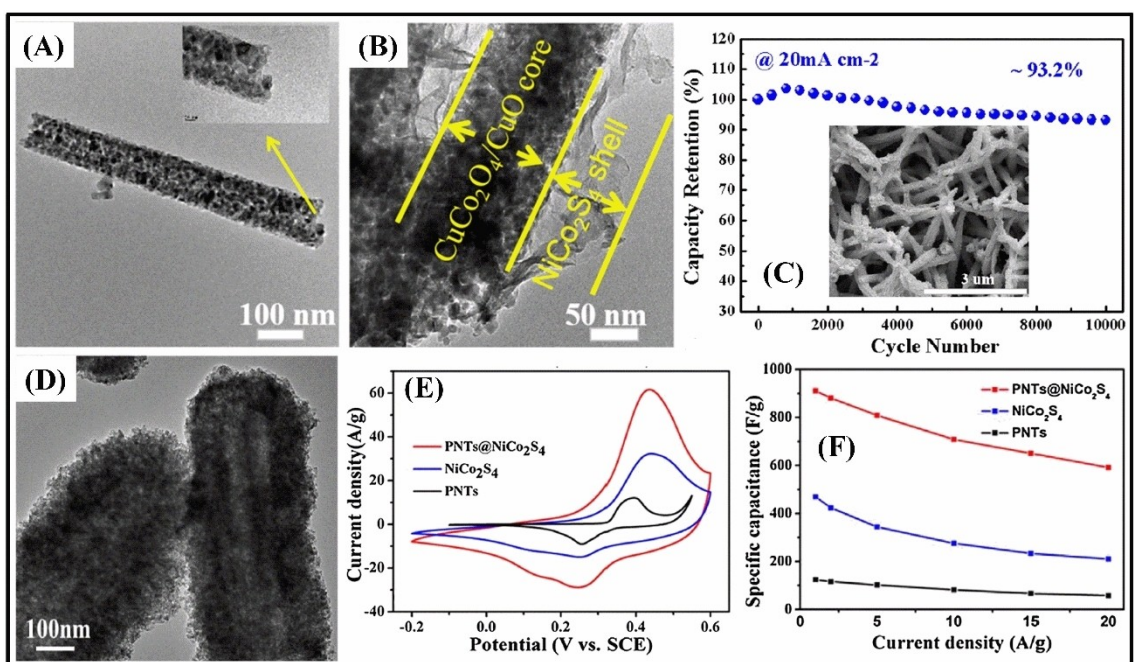


Figure 11. TEM images of CuCo₂O₄/CuO and CuCo₂O₄/CuO/NiCo₂S₄ (A and B). Capacity retention vs. cycle number (C). Reproduced from Ref. [48] with permission. Copyright (2019) Elsevier B.V. TEM image of hierarchical PNTs@NiCo₂S₄ core@shell structured material (D). Cyclic voltammograms of PNTs@NiCo₂S₄, NiCo₂S₄, and PNTs electrodes (E) and respective specific capacitances (F g⁻¹) as a function of current density (A g⁻¹) (F). Reproduced from Ref. [51] with permission. Copyright (2017) Elsevier Ltd.

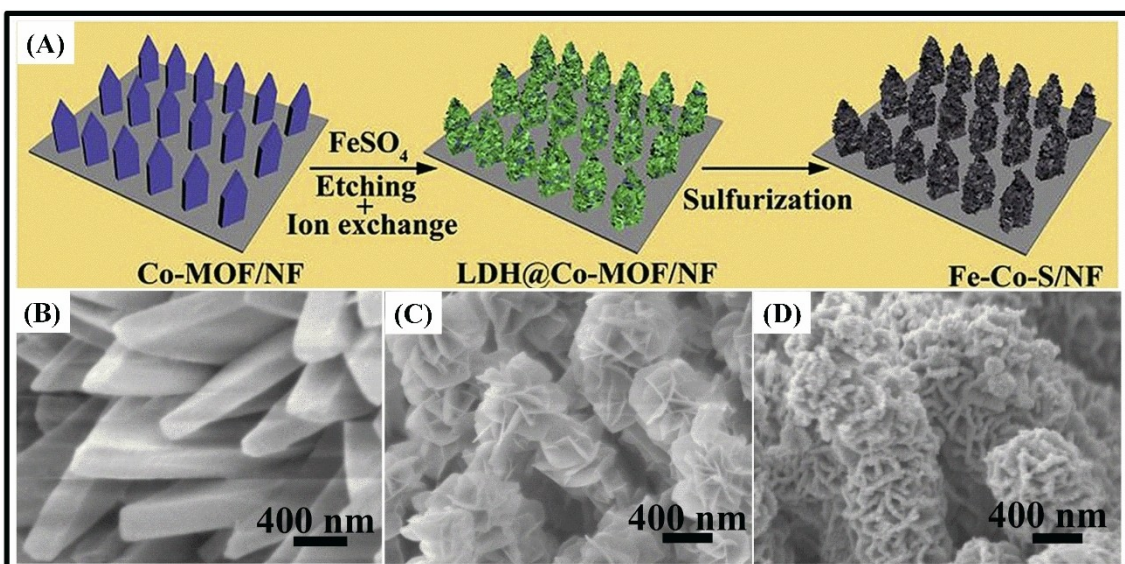


Figure 12. A) Schematic illustration of the fabrication steps of $\text{Co}_3\text{S}_4@\text{FeCo}_2\text{S}_4/\text{NF}$. B) SEM images of Co-MOF/NF, C) Co-MOF@FeCo-LDH/NF and D) $\text{Co}_3\text{S}_4@\text{FeCo}_2\text{S}_4/\text{NF}$. Reproduced from Ref. [54] with permission. Copyright (2019) Elsevier Ltd.

electrode presented specific capacitance of 1500 F g^{-1} at 1 Ag^{-1} , with a rate capability of 36.3% at 10 Ag^{-1} , and capacitance retention of 70% after 1000 cycles. The assembled $\text{Co}_3\text{S}_4@\text{FeCo}_2\text{S}_4/\text{NF}/\text//\text{rGO}$ ASC delivered 131 F g^{-1} at 1 Ag^{-1} and presented a rate capability of 81.5% at 10 Ag^{-1} , along with a calculated maximum power and energy densities respectively of 43.6 Wh kg^{-1} (at 770 W kg^{-1}) and 5510 W kg^{-1} (at 13.3 Wh kg^{-1}), and a capacitance retention of 89.6% after 5000 cycles, demonstrating its high potential for practical application.

Overall, the $\text{Co}_3\text{S}_4@\text{FeCo}_2\text{S}_4/\text{NF}$ electrodes presented many outstanding advantages that improved their properties as SC electrode materials, such as superior specific surface area and pores for electrolyte diffusion. These features enlarge the electrode/electrolyte contact area, increases the accessibility of electrochemical active sites and better accommodate the double-layer charges, enhancing the electronic conductivity and the density of redox sites ($\text{Fe}^{2+}/\text{Fe}^{3+}$ and $\text{Co}^{2+}/\text{Co}^{3+}$) of FeCo_2S_4 . Finally, the strong adhesion of the electrode material on NF ensured a good rate capability and cycling stability.

5.3. Bimetallic Sulfides as Core and Shell Materials

Interestingly, some works reported in the literature described 3D core@shell hierarchical structures based on bimetallic sulfides as both, core and shell. In this perspective, Ma *et al.*^[58] produced $\text{CuCo}_2\text{S}_4@\text{NiCo}_2\text{S}_4$ on NF by growing mesoporous CuCo_2S_4 nanoneedle arrays core directly on NF by hydrothermal process and uniformly covering it with NiCo_2S_4 nanosheets arrays deposited on the top by a second hydrothermal processing, resulting in a 3D coralline-like $\text{CuCo}_2\text{S}_4@\text{NiCo}_2\text{S}_4$ nanostructured material (Figure 13). The morphologies of all three materials are presented in the SEM images of CuCo_2S_4 nanoneedles arrays (Figure 13A), NiCo_2S_4 nanosheets (Fig-

ure 13B), and the $\text{CuCo}_2\text{S}_4@\text{NiCo}_2\text{S}_4$ core@shell material (Figure 13C–13D). The shell of NiCo_2S_4 nanosheet arrays allow a higher density of redox sites and higher specific capacity while significantly increasing the contact area with the electrolyte and protecting the CuCo_2S_4 nanoneedle arrays core during the charge-discharge processes. This structuration is interesting since it has lower electrochemical stability but larger conductivity. The $\text{CuCo}_2\text{S}_4@\text{NiCo}_2\text{S}_4$ electrode delivered a specific capacity of 537.2 C g^{-1} at 1 Ag^{-1} with capacity retention of 74.5% until current densities up to 8 Ag^{-1} , and 100% retention up to 5000 cycles. On the other hand, CuCo_2S_4 and NiCo_2S_4 electrodes delivered 363 and 378.12 C g^{-1} at 1 Ag^{-1} . The all-solid-state asymmetric $\text{CuCo}_2\text{S}_4@\text{NiCo}_2\text{S}_4/\text//\text{AC}$ supercapacitor device delivered 120 F g^{-1} at 1 Ag^{-1} and about 65% of capacitance retention at 5 Ag^{-1} , and maintained 71% of its initial specific capacitance after 3000 cycles. Furthermore, the highest energy density and power density of the ASC device were respectively 23.4 Wh kg^{-1} at 400 W kg^{-1} and 4000 W kg^{-1} at 12.5 Wh kg^{-1} .

The good electrochemical properties presented by the $\text{CuCo}_2\text{S}_4@\text{NiCo}_2\text{S}_4$ electrode were ascribed to the better electron-transfer rate to the current collector due to the direct growth of CuCo_2S_4 nanoneedles core directly on NF, superior electrochemical capacity and higher electrochemical stability provided by the NiCo_2S_4 nanosheets shell protecting the core material, superior specific surface area, availability of active sites and ion-diffusion rates due to coralline-like core@shell structures, and rich Faradaic redox reactions due to the presence of multivalence metallic ions ($\text{Co}^{2+}/\text{Co}^{3+}$ and $\text{Ni}^{2+}/\text{Ni}^{3+}$) as electrochemically active sites in NiCo_2S_4 .

Similarly, Yu, Tang and Dai^[56] synthesized double-layer $\text{MnCo}_2\text{S}_4@\text{NiCo-S}$ on NF by growing needle-like MnCo_2O_4 nanorods directly on NF by hydrothermal method and annealing, followed by sulfurization process to transform it into corncob-like MnCo_2S_4 nanorods, used as core for the uniform growth of

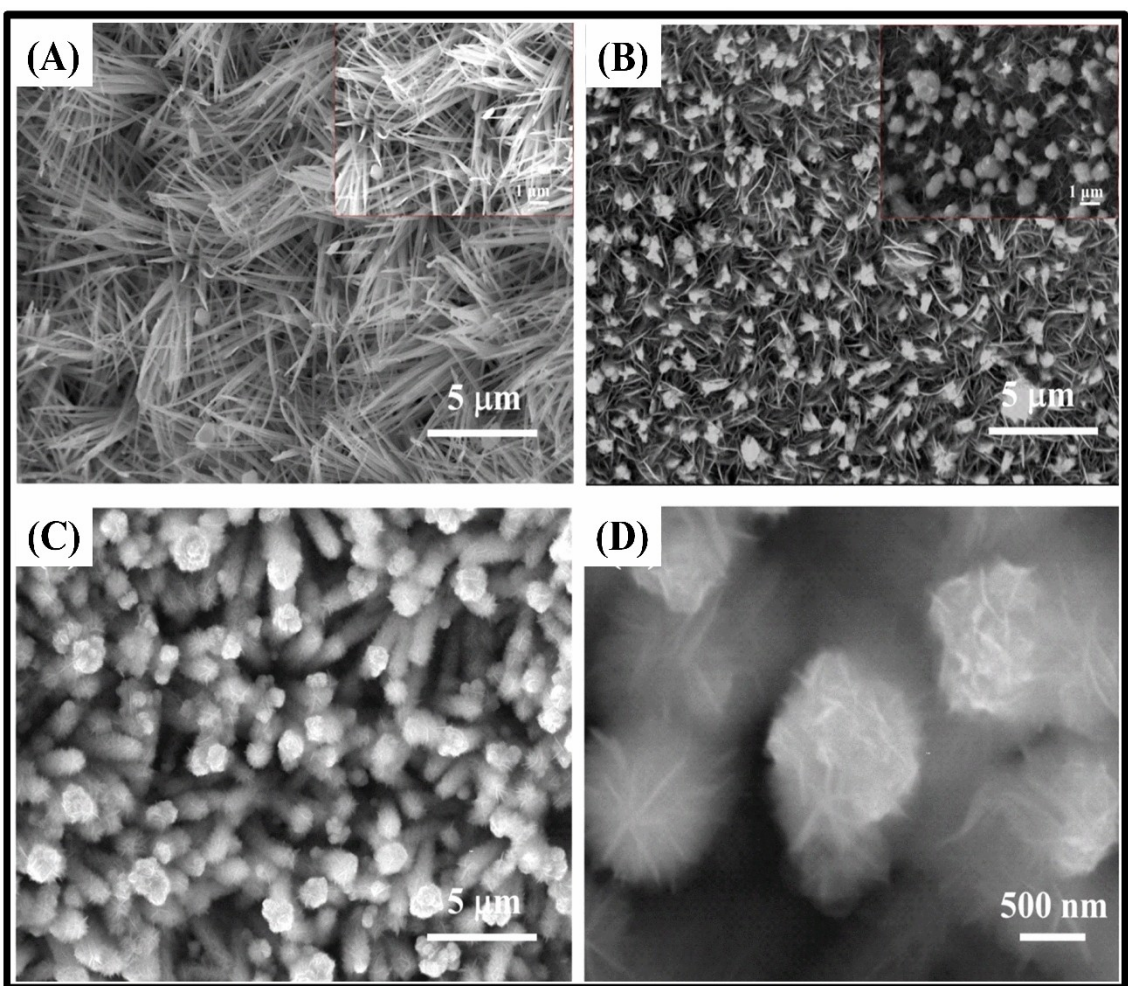


Figure 13. A–C) SEM images of the CuCo₂S₄ nanoneedles arrays, NiCo₂S₄ nanosheets, CuCo₂S₄@NiCo₂S₄ composites, and D) enlarged view of (C). Reproduced from Ref. [58] with permission. Copyright (2019) IOP Publishing.

NiCo-S nanosheets on its surface by electrodeposition (Figure 14A). These structures can be seen in the SEM and TEM images, in which it is possible to observe needle-like MnCo₂O₄ nanorods (Figures 14B and 14E), corncob-like MnCo₂S₄ nanorods (Figures 14C and 14F) and the MnCo₂S₄@NiCo-S core/shell material (Figures 14D and 14G). The MnCo₂S₄@NiCo-S/NF electrode achieved areal and specific capacitances of 10.14 F cm⁻² and 2668.4 F g⁻¹ at 1 mA cm⁻², and was able to retain 82.3% of this value at 20 mA cm⁻². The electrode also delivered 62.7% of its initial capacitance after 3500 cycles, that remained constant up to 5000 cycles. The more or less constant decrease rate in the capacitance was ascribed to the collapse of some core@shell structures during the charge/discharge processes. In comparison, MnCo₂O₄ and MnCo₂S₄ electrodes presented significantly much lower areal capacitances, respectively of 2.71 and 5.23 F cm⁻² at 1 mA cm⁻². Furthermore, the ASC fabricated using MnCo₂S₄@NiCo-S/NF as the positive electrode and activated carbon on NF (AC/NF) as the negative electrode delivered 1.92 F cm⁻² at 1 mA cm⁻², rate capability of 60% at 20 mA cm⁻² and 72% capacitance retention after 5000 cycles, as well as maximum energy density of 30.5 Wh kg⁻¹ at

35 W kg⁻¹ and maximum power density of 683.7 W kg⁻¹ at 19 Wh kg⁻¹.

MnCo₂S₄@NiCo-S/NF electrodes superior performance can be explained by the high specific surface area and mesoporous corncob-like structure, which minimize the ionic diffusion pathway and enhance the accessibility to the active-sites. The multivalence ions Co²⁺/Co³⁺, Ni²⁺/Ni³⁺ in NiCo-S shell and Mn²⁺/Mn³⁺, Co²⁺/Co³⁺ in MnCo₂S₄ core materials boost the density of Faradaic reaction sites and increases the redox activity, especially in the shell, due to the increased electrochemical activity of Ni-S. And, the higher electrical conductivity of MnCo₂S₄ core material, given the presence of Mn-S, facilitates the electron transport and current collection.

Ma *et al.*^[55] reported the synthesis of a core@shell structure based on CoMoS₄@NiCo-S. The CoMoS₄ core material was obtained by hydrothermal method, whereas the shell material (NiCo-S) was deposited electrochemically on the top of the core material. The TEM image of CoMoS₄@NiCo-S displayed in Figure 15A reveals the formation of CoMoS₄ nanotubes with NiCo-S nanosheets anchored on the surface, forming ~220 nm diameter core@shell structure. The electrochemical studies of the CoMoS₄@NiCo-S showed the material presents two types of

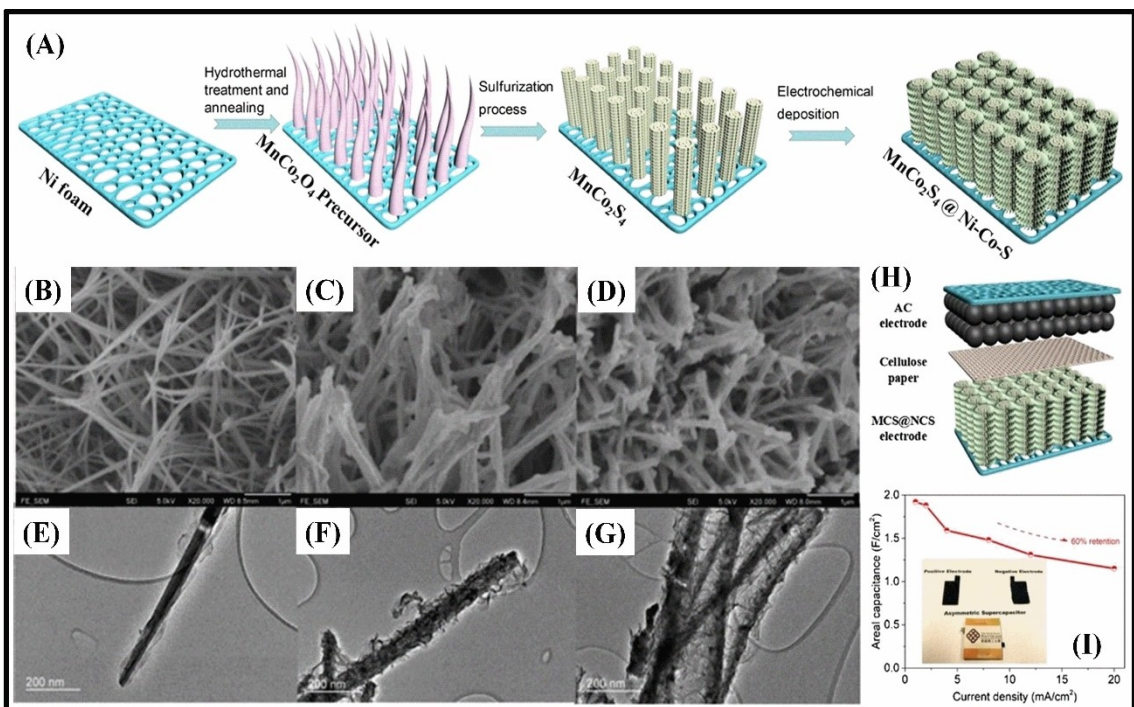


Figure 14. A) A schematic illustration of the fabrication process of the $\text{MnCo}_2\text{S}_4@\text{NiCo-S}$ core@shell nanocomposite on Ni foam. SEM images of B) MnCo_2O_4 , C) MnCo_2S_4 and D) $\text{MnCo}_2\text{S}_4@\text{NiCo-S}$. TEM images of E) MnCo_2O_4 , F) MnCo_2S_4 , and G) $\text{MnCo}_2\text{S}_4@\text{NiCo-S}$. H) Schematic diagram of the asymmetric supercapacitor assembled with AC electrode. I) Areal capacitance of the ASC as a function of current density. The digital image of the electrodes and ASC are shown in the inset. Reproduced from Ref. [56] with permission. Copyright (2018) Wiley-VCH Verlag GmbH & Co. KGaA.

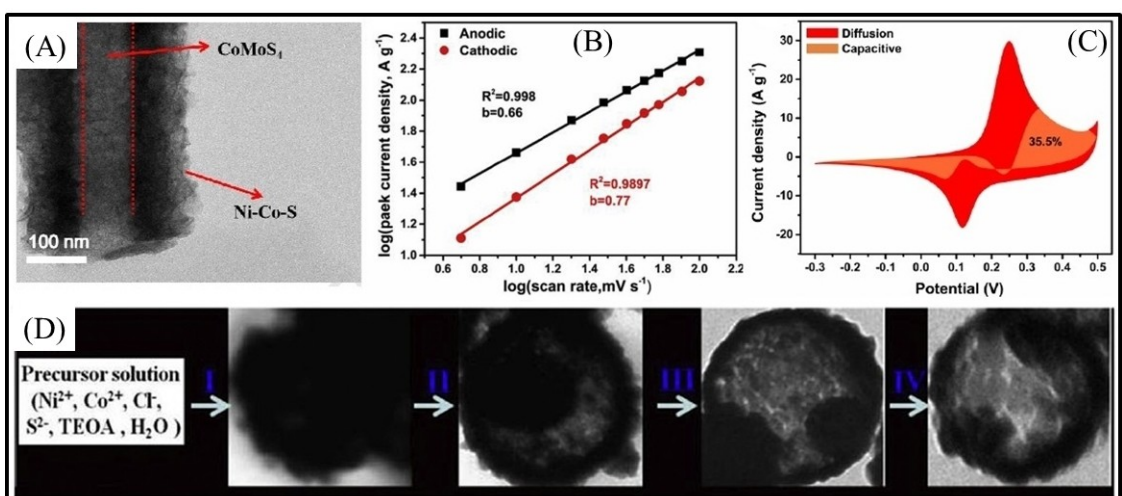


Figure 15. TEM image of $\text{CoMoS}_4@\text{NiCo-S}$ (A), Logarithm relationship between peak current density and scan rate (B). Capacitance-controlled and diffusion-controlled contribution to charge storage capacity at 5 mV s^{-1} (C). Reproduced from Ref. [55] with permission Copyright (2019) Elsevier Ltd. TEM images of solid (I), hollow core@shell (II and III) and hollow nanosphere (IV). Reproduced from Ref. [33b] with permission Copyright (2017) Elsevier B.V.

charge storage mechanisms that can be identified by comparing the slope of the $\log i$ vs \log (sweep rate) curve in Figure 15B. A slope of 0.5 indicates a diffusion controlled Faradaic process whereas a slope of 1.0 is characteristic of a capacitive process. In this case, the slopes were 0.66 and 0.77 for the anodic and the cathodic peak, suggesting the contribution of both charge storage mechanisms. Their contribution to the charge storage capacity was determined by the

Dunn's method^[61] using the equation $i(V) = k_1v + k_2v^{1/2}$, where k_1v corresponds to the capacitive contribution and $k_2v^{1/2}$ to the Faradaic contribution, that were found to be respectively 35.5% and 64.5% at a scan rate of 5 mV/s , as shown in Figure 15C. These results demonstrate that the main charge storage mechanism is driven by diffusion controlled redox processes, typical of battery-type materials. The $\text{CoMoS}_4@\text{NiCo-S}$ electrode presented an excellent capacity retention of 91.3%

after 5,000 cycles, and a rate capability of 68.8% from 1 to 20 mA cm⁻². Similar results were reported by Yu, Tang and Dai^[56] that prepared MnCo₂S₄@NiCo-S on nickel foam substrate by a hydrothermal method followed by electrodeposition. The resultant MnCo₂S₄@NiCo-S electrode showed a capacitance of 10.14 F cm⁻² at 1 mA cm⁻², as well as a good rate capability of 82.3% from 1 to 20 mA cm⁻². Such an exceptional performance can be assigned to two main aspects: (i) the core material works as a good current collector and facilitate the electron transport because of its high electrical conductivity, and (ii) the shell material with its multifarious redox reactions can provide a high pseudo-capacitance.

In addition to nanotubes, nanorods and nanowires, and other interesting structures such as hollow core@shell nanospheres, has been designed using bimetallic sulfides. Liang *et al.*^[33b] for the first time reported the synthesis of CoNi₂S₄ nanospheres in a hollow core@shell structure by a hydrothermal method. The authors noticed that both the reaction time and the triethanolamine (TEOA) concentration influence the formation of hollow core@shell nanospheres. In the absence the TEOA the product is a mixture of CoNi₂S₄ and NiS, whereas pure CoNi₂S₄ is formed as product in the presence of 0.1 to 0.6 g of TEOA. However, the product can be shifted to almost pure hollow core@shell structured material by optimizing the amount of TEOA. In addition, the authors noticed that only solid CoNi₂S₄ nanospheres are formed when the reaction was stopped after 1 hour, as shown in Figure 1D (I). However, when the reaction is interrupted after 4 hours, a well-defined shell and a solid core were obtained, as depicted in Figure 15D (II and III). Interesting enough, after longer reaction times (12 h), the solid core vanished forming a single shell hollow structure, Figure 15D (IV). The electrochemical behavior of hollow CoNi₂S₄ nanospheres was evaluated and presented a specific capacitance of 2035 F g⁻¹ at 1 Ag⁻¹, a rate capability of 59.7% from 1 to 20 Ag⁻¹, and a good cycling stability of 91.3% after 3,000 cycles.

5.4. Trimetallic Sulfides as Core@Shell Structures

As discussed in the previous chapter, bimetallic sulfides have superior conductivity and electrochemical activity for energy storage applications and richer redox properties than their monometallic counterparts due to synergistic effects induced by the partial substitution of their metal ion. For example, bimetallic sulfides based on nickel and cobalt ions (e.g., NiCo₂S₄) are known for their higher specific capacitance in comparison to their monometallic counterparts and electrical conductivity larger than of NiCo₂O₄,^[62] as well as enhanced redox properties than the corresponding single-phase sulfides,^[63] exhibiting even better performances in core@shell systems. Nevertheless, they present some downsides, such as limited capacitance and short life cycle. Many approaches can be applied to overcome such limitations, but two stand out among them and deserves much attention: 1) the design of core@shell structured materials based on those bimetallic sulfides, as seen in the previous chapter; and 2) the incorpo-

ration of another metal ion into the sulfide structure, producing a trimetallic sulfide,^[8b,10,30,58,64] for example by substituting some of its cations by Mn,^[64a,b] Mo,^[64d] Cu^[30] or Fe.^[8b,64c]

As recently reviewed by our group,^[3a] mixed metallic oxides based on three different transition metals have several advantages and enhanced electrochemical properties in comparison with their respective mono- and bimetallic counterparts, provided basically by their multiple oxidation states and higher density of active sites.^[8b,10,30,54,58,64] The combination of three different metal ions by morphologic and composition control can promote numerous synergistic effects that can enhance the electronic conductivity, ion diffusion rate, electrochemical activity and mechanical and chemical stability, while lowering the activation energy for electron-transfer between the metal centers. In fact, metal sulfides demonstrate similar redox reactions and provide even better electrical conductivity, mechanical and thermal stability, and higher electrochemical activity than their metal oxide counterparts.^[8b,10,30,64] Accordingly, trimetallic sulfides are promising materials for energy storage applications.^[8b,10,30,64] However, even though trimetallic sulfides can be superior electrode materials for supercapacitors as compared to mono- and bimetallic sulfides and to trimetallic oxides, only few studies have been carried out on the subject.

Many core@shell structures have been designed with bimetallic sulfides as either core or the shell, or both, where the core material presents high conductivity and the shell high specific capacitance. From this perspective, by applying the benefits of core@shell structures with the enhanced synergistic effects of trimetallic sulfides over bimetallic sulfides it is possible to obtain even better electrode materials for application in supercapacitors, with higher electrical conductivity, charge transfer/diffusion rates, specific capacitance and/or even electrochemical stability due to the many possible synergistic effects.^[8b,10,30,64] Trimetallic sulfides can be designed as core and/or shell, since the variety of morphologies and compositions provides specific synergistic properties depending on the interaction of both parts. Table 3 presents the specific properties of all trimetallic sulfide-based core@shell materials for supercapacitor application found in the literature in the recent years.

Core@shell materials grown as ultrathin materials on highly conductive substrates present improved charge-transfer and electrical conductivity. Therefore, additionally to the trimetallic sulfide-based core@shell materials,^[30] recent reports indicate hierarchical materials prepared with trimetallic sulfides as core and *in situ* grown mixed transition metal hydroxides shell can be an efficient strategy to exploit the relatively larger conductivity and specific capacitance of these materials, respectively.^[8b,64b,d] Interestingly, since trimetallic sulfides have even higher electrochemical activity in comparison to the mono- and bimetallic counterparts, they are promising as shell materials along with a core prepared with an even more conductive material, such as carbon nanotube fibers (CNTF)^[64a] and nickel nanocone arrays (NCA).^[64c]

The superior electrochemical performance of core@shell materials with trimetallic sulfides as core can be attributed to synergistic effects encompassing:^[30,64b,d,65] 1) the enhanced sur-

Table 3. Comparison of the relevant electrochemical parameters of trimetallic sulfide core@shell-based materials and their performance in energy storage devices assembled with a suitable cathode material. ^[a]								
Materials	Specific capacitance [$F\text{g}^{-1}$]	Potential window	Rate capability [Ag^{-1}] (retention [%])	Durability (charge retention [%])	Highest energy density [Whkg^{-1}]	Highest power density [Wkg^{-1}]	Cathode material Core	Synthesis methods Shell
Core	3D hollow Cu(NiCo) ₂ S ₄ @Ni ₃ S ₄ microflowers on NF	Three electrode system SC device	1320 at 1 Ag^{-1} 1206 at 1 Ag^{-1}	0.0–0.5 V vs. Hg/HgO 0.0–1.6 V	1–20 (75) 1–20 (66.3)	5000 cycles (75) 5000 cycles (84.9)	40.8 at 785.5 Wkg^{-1} 2000 cycles (159.4)	7859.2 at 27.1 Whkg^{-1}
	Ni _{1.80} Co _{0.50} Mn _{0.50} S _{1.52} @NiCoMn-OH nanoneedles on NF	Three electrode system SC device	136 mAhg ⁻¹ at 5 mV s^{-1}	0.0–0.6 V vs. Hg/HgO				HT EA [64b]
3D MoCoNi-S@NiCo-OH nanopine forest arrays on CC	Three electrode system SC device	1998 and 9.81 Fcm^{-2}		−0.2–0.5 V vs. Hg/HgO	1–20 (83)	3000 cycles (85.4)		HT ED [64d]
	NiFeCo-S@NiFeCo-OH on NiF	Three electrode system SC device	(9.56 Fcm^{-2}) 174 mAhg ⁻¹ at 10 mA cm^{-2}	0.0–0.4 V vs. SCE (83)	10–100 (mA cm^{-2}) (68.3)		56.3 at 543 Wkg^{-1} 3500 at 28.3 Whkg^{-1}	AC EO and two-step HT [65]
Shell	Self-supported CNTF@MnNiCo-S multi-tripod nanotube arrays	Three electrode system SC device	57.2 mAhg ⁻¹ at 10 mA cm^{-2} 2554.5 Fcm^{-3} (7.03 Fcm^{-2}) at 1 mA cm^{-2}	0.0–1.6 V 0.0–0.4 V vs. SCE	10–150 (mA cm^{-2}) 1–10 (84.6)	4000 cycles (90.1) 5000 cycles (94.8)	3500 at 28.3 Whkg^{-1} 52.4 mWh cm^{-3} (144 $\mu\text{Wh cm}^{-2}$) at 582 Wcm^{-3}	AC EO and two-step HT [64a]
	NCA@NiCoFe-S on NP	Three electrode system SC device	147 Fcm^{-3} (405 mF cm^{-2}) at 2 mA cm^{-2} 2159.7 at 7 Ag^{-1}	0.0–1.6 V 0.0–0.43 V vs. Ag/AgCl	2–15 (62.7) 7–35 (67.7)	5000 cycles (92.9) 1000 cycles (92)	35.9 at 375 Wkg^{-1} 7500 at 6.9 Whkg^{-1}	VN HT IE [64c]
		SC device	114 at 0.2 Ag^{-1}	0.0–1.5 V	0.2–10 (~26)		rGO	ED ED

[a] SC: supercapacitor; NF: nickel foam; AC: active carbon; HT: hydrothermal; IE: ion-exchange; CNTF: carbon nanotube fibers; SCE: saturated calomel electrode; PC: porous carbon; CF: porous carbon; VN: vanadium nitride; EA: electrochemical activation; NCA: nickel nanocone arrays; NP: nickel nanocone arrays; CC: carbon cloth; NIF: nickel-ion foam; EO: electrochemical oxidation.

face area due to the hierarchical structures, which leads to larger electrolyte/electrode interfaces and promotes facile electrolyte diffusion; 2) increased mechanical and electrochemical stability provided by the tight contact between the electrode components due to the *in-situ* synthesis; 3) abundant redox active sites and rapid transport of ions/electrons, provided by numerous edge sites and the ultrathin interfaces with strong affinity for OH⁻; 4) enhanced conductivity, high charge storage efficiency and rich electrochemical properties due to the multi-metallic multivalence character (Ni³⁺/Ni²⁺, Co³⁺/Co²⁺ Cu²⁺/Cu⁺,^[30] Mn²⁺/Mn³⁺,^[64a,b] Mo⁴⁺/Mo⁵⁺/Mo⁶⁺^[64d] and Fe²⁺/Fe³⁺)^[64c,65] of all reported materials in each specific case.

5.5. Trimetallic Sulfides as Core Materials

Zhao *et al.*^[66] studied the synergic effects of trimetallic sulfides in an all-sulfide core@shell electrode material with a trimetallic sulfide as core and monometallic sulfide as shell. More specifically, they prepared 3D hierarchical hollow Cu_{(NiCo)₂S₄}@Ni₃S₄ microflowers on NF by first producing Cu_xCo_{2-x}-MOF by a hydrothermal method followed by an ion-exchange step to produce CuNiCo-OH and by another hydrothermal processing to produce hollow Cu(NiCo)₂S₄@Ni₃S₄ microflowers, which inherited this structure from the bimetallic-MOF precursor (Figure 16A). The trimetallic sulfide petal-like sheets presents larger pores (5–10 nm) in comparison to its precursors due to the anion exchange steps, and numerous cross-connected nanoparticles on its surface, with abundant space between neighboring structures (Figure 16B–16E).

CuNiCo-OH and Cu(NiCo)₂S₄@Ni₃S₄ electrodes achieved 670 and 1320 F g⁻¹ at 1 A g⁻¹, respectively, retaining 46% and 75.7% of capacity at 20 A g⁻¹ (Figure 16F). As for long-term cycling stability, 75% of Cu(NiCo)₂S₄@Ni₃S₄ initial capacitance was retained after 5,000 GCD cycles. A hybrid supercapacitor (HSC) device was assembled using AC as negative electrode to investigate its potentiality for practical application. The HSC device delivered 120.6 F g⁻¹ at 1 A g⁻¹, with 66.3% capacitance retention at 20 A g⁻¹, long-term stability retaining 85% of capacitive and 95.2% of coulombic performance after 5,000 cycling tests. Also, exhibited highest energy density of 40.8 Wh kg⁻¹ at the power density of 785.5 W kg⁻¹, while delivering 27.1 Wh kg⁻¹ at the highest power density of 7,859.2 W kg⁻¹.

The superior electrochemical performance presented by 3D hierarchical hollow Cu(NiCo)₂S₄@Ni₃S₄ microflowers on NF electrodes was attributed to the already discussed shared synergistic effects. The large surface area and hierarchical porous structure provided by the tightly stacked 5–10 nm nanopetals, serving as 3D channels for fast and optimal electrolyte ion/electron diffusion, facilitates the electrolyte penetration and buffered the strain resulting from the rapid intercalation/de-intercalation of OH⁻ ions. In addition, high concentration of electrochemically active sites are available given the increased roughness and cross-connected nanoparticles on the nanopetals surface (Figure 16G). Furthermore,

the electrodes presented superior electrochemical stability capable to sustain thousands of charge/discharge processes given the stable bimetallic-MOF derived microflower structure, as well as enhanced conductivity and multivalence and multi-metallic nature provided by the Cu²⁺/Cu⁺, Ni³⁺/Ni²⁺ and Co³⁺/Co²⁺ redox couples.

Only three materials that can be classified as mixed transition metal sulfide-hydroxide core@shell materials were found in the literature: Ni_{1.80}Co_{0.50}Mn_{0.50}S_{1.52}@NiCoMn-OH nanoneedles,^[64b] 3D MoCoNi-S@NiCo-OH nanopine forest arrays,^[64d] and hierarchical petal-like NiFeCo-S@NiFeCo-TH heterogeneous ultrathin nanosheets.^[65] Sanchez *et al.*^[64b] prepared Ni_{1.80}Co_{0.50}Mn_{0.50}S_{1.52}@NiCoMn-OH nanoneedles on NF by growing the Ni_{1.80}Co_{0.50}Mn_{0.50}S_{1.52} core material directly on NF by a facile two-step hydrothermal method, and subsequently formation process of NiCoMn-OH shell structure during potential cycling. The core@shell material was characterized by *in operando* Raman measurements realized during the synthesis (Figures 17C–17D), as well as *ex-situ* XRD (Figures 17B), dark-field STEM (Figures 17F and 17J) and elemental mapping for S and O atoms (Figures 2G–2H and Figures 2K–2L). Elemental line scans (Figure 17I and Figure 17M) of a single Ni_{1.80}Co_{0.50}Mn_{0.50}S_{1.52}@NiCoMn-OH NCMS nano-needle, before and after redox cycling, revealed a rough, thick layer of amorphous nanosheets of NiCoMn-OH shell covering the smooth and homogeneous 100 nm thick nanoneedle cores of Ni_{1.80}Co_{0.50}Mn_{0.50}S_{1.52}, giving rise to a core@shell material suffering quasi-reversible sulfide/hydroxide conversion for up to 2,000 CV cycles in alkaline media (Figures 17A and 17E). In fact, Ni_{1.80}Co_{0.50}Mn_{0.50}S_{1.52}@NiCoMn-OH were unintendedly produced after the characterization of Ni_{1.80}Co_{0.50}Mn_{0.50}S_{1.52} and (Ni_{1-(x+y)}Co_xMn_y)OH₂, Ni_{1.80}Co_{0.50}Mn_{0.50}S_{1.52} and Ni_{1.80}Co_{0.50}Mn_{0.50}S_{1.52}@NiCoMn-OH calculated from the CVs were respectively 48, 136 and 220 mAh g⁻¹ at 5 mV s⁻¹. Interestingly, the specific capacity of Ni_{1.80}Co_{0.50}Mn_{0.50}S_{1.52} increased during the electrochemical activation process and reached an almost steady value after 2,000 cycles, when Ni_{1.80}Co_{0.50}Mn_{0.50}S_{1.52}@NiCoMn-OH was finally formed (Figures 17A and 17F), indicating the superior performance of core@shell materials based on metal sulfides-hydroxides as compared to the individual constituent materials. The unique structure presented by the nanostructured material not only benefits from the superior charge storage capacity of the trimetallic hydroxide, which unfortunately is not discussed in the article, but also the enhanced electrode/electrolyte interface and accessible active-sites while decreasing the ion-diffusion path-lengths. In fact, these results show that despite the instability of sulfides during electrochemical processing in an alkaline environment, the *in situ* formation of sulfide@hydroxide core@shell structures is an interesting strategy to prepare very promising electrode materials for energy storage purpose.

Despite these interesting results, the authors assembled an all-solid-state ASC device using only the precursor trimetallic

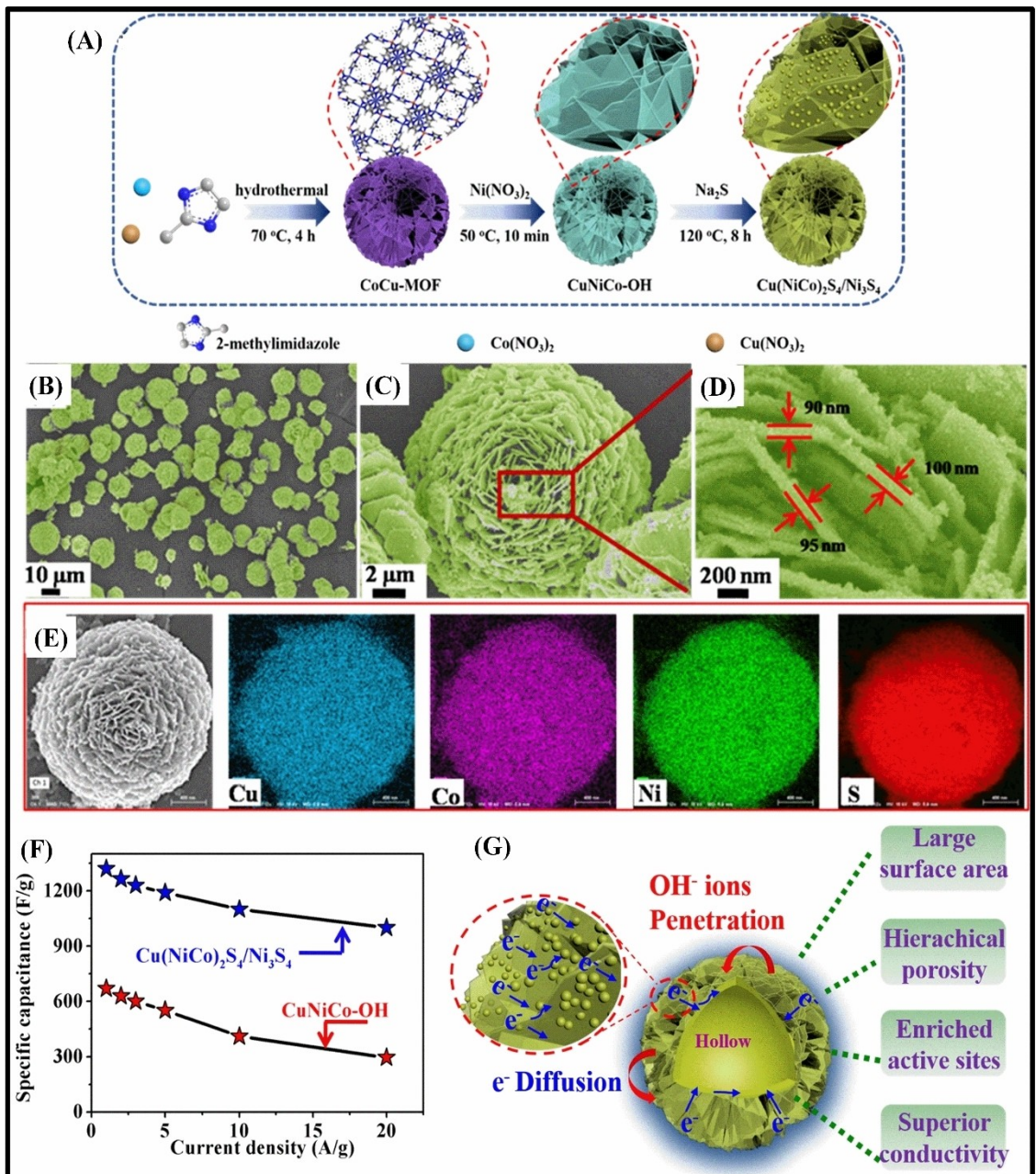


Figure 16. A) Schematic illustration of the fabrication steps of $\text{Cu}_{x}\text{Co}_{2-x}$ -MOF and the 3D hierarchical hollow $\text{Cu}(\text{NiCo})_2\text{S}_4/\text{Ni}_3\text{S}_4$ microflowers by sequential *in-situ* ion exchange reactions. B-D) SEM images of $\text{Cu}(\text{NiCo})_2\text{S}_4/\text{Ni}_3\text{S}_4$ and E) the corresponding elemental mapping images. F) Specific capacitances of $\text{Cu}(\text{NiCo})_2\text{S}_4/\text{Ni}_3\text{S}_4$ and CuNiCo-OH as a function of current density. G) Schematic illustration of $\text{Cu}(\text{NiCo})_2\text{S}_4/\text{Ni}_3\text{S}_4$ electrode and charge storage mechanism. Reproduced from Ref. [66] with permission. Copyright (2020) Elsevier Inc.

sulfide and rGO respectively as cathode and anode, and shallowly discussed the electrochemical properties of more promising $\text{Ni}_{1.80}\text{Co}_{0.50}\text{Mn}_{0.50}\text{S}_{1.52}$ @NiCoMn-OH as electrode material. Therefore, urge more in depth electrochemical characterization, assembly and study of SC devices for evaluation of the practical usage potential are highly encouraged.

Lv *et al.*^[64d] on the other hand, explored deeply the synergistic effects of core@shell materials based on transition metal sulfides-hydroxides. They prepared 3D MoCoNi-S@NiCo-OH nanopine forest arrays on carbon cloth (CC) by growing the

core directly on CC by a two-step hydrothermal method, and the shell by electrodeposition (Figure 18A–18D). First, the trimetallic sulfide core nanowires were directly grown on the nanosheets (Figure 18B), transformed into rough hollow nanotubes via vulcanization (Figure 18C), and used as backbone of thin, short and sparse trimetallic hydroxide nanosheets shell, forming a pine forest-like structure (Figure 18D). The structure of all materials was confirmed by typical SEM images at different magnifications (Figures 18E–18H and Figures 18I–18L), whereas FEG-TEM images (Figure 18M) and its corresponding

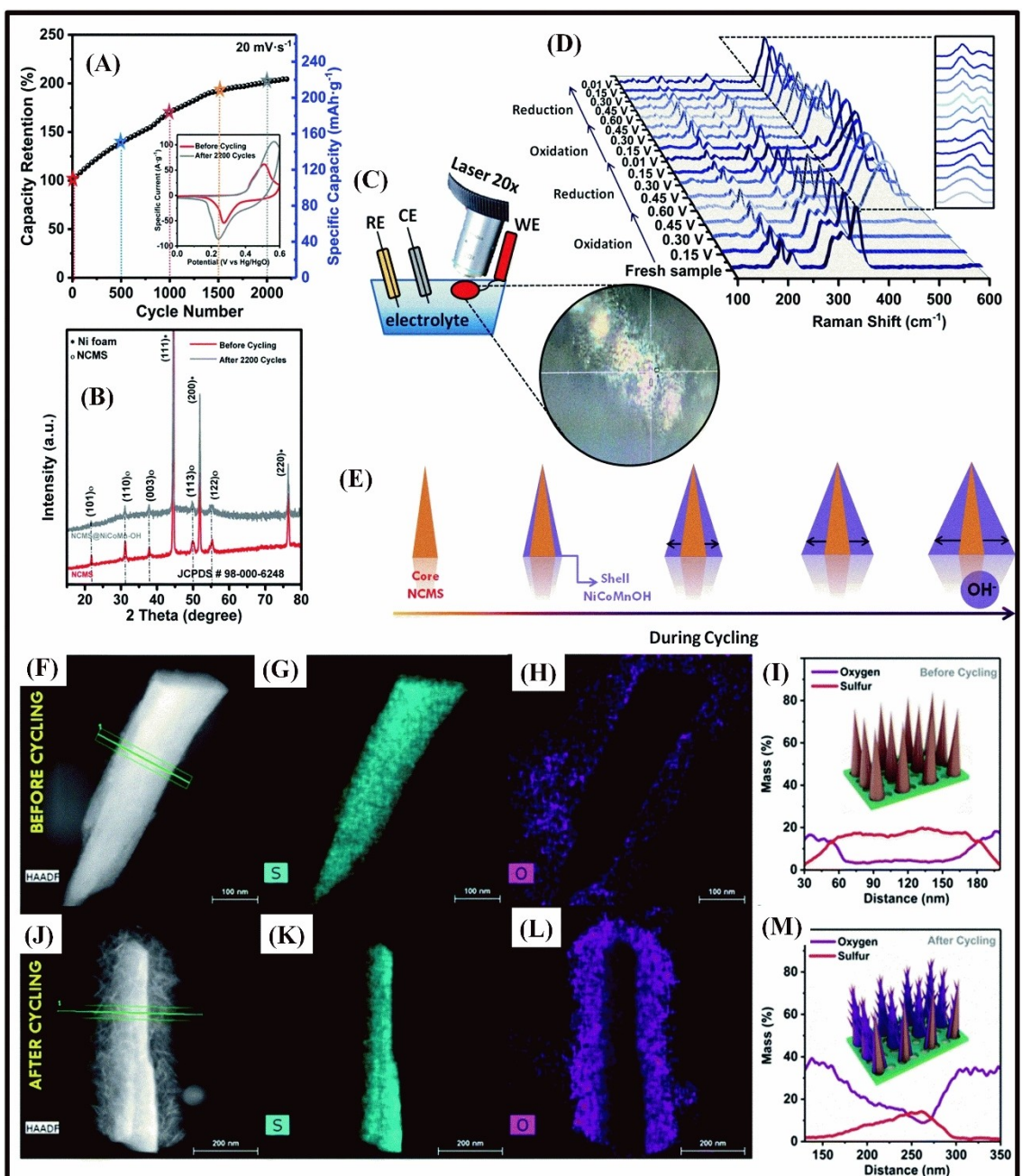


Figure 17. A) Charge retention capacity of NCMS as a function of the number of cycles at 20 mV s^{-1} , using a three-electrodes cell configuration, and the CVs before and after 2,200 cycles (inset). B) XRD patterns before and after redox cycling; C) Schematic representations of *in operando* Raman setup along with the acquired optical image. D) *In operando* Raman spectra of the NCMS electrode collected during oxidation and reduction in two consecutive redox cycles. E) Schematic illustration of the formation of NCMS@NiCoMn-OH hierarchical core@shell structure in the course of cycling. F) Dark-field STEM image of a single NCMS nano-needle before cycling and G, H) its corresponding STEM elemental mappings for S and O. I) Elemental line scans across the NCMS nanoneedle before cycling. J) Dark-field image of a NCMS nanoneedle after cycling and K, L) its corresponding STEM elemental mappings; M) Elemental line scans across the NCMS nanoneedle after cycling. The inset shows a schematic representation of the core@shell structure formation. Reproduced from Ref. [64b] with permission. Copyright (2019) Royal Society of Chemistry.

elemental mapping images (Figures 18N–18R) were carried out for 3D MoCoNi-S@NiCo-OH nanopine forest arrays on CC to further confirm the core/shell structure. The specific and areal capacitances of the 3D MoCoNi-S@NiCo-OH electrode are respectively 1998 F g^{-1} and 9.81 F cm^{-2} at 1 mA cm^{-2} , with a rate capability of 83% at 10 mA cm^{-2} and capacitance retention of 85.4% after 3,000 cycles, in contrast with the precursor

MoCoNi nanowire arrays, MoCoNi-S nanotube arrays and NiCo-OH nanosheet arrays electrodes that presented areal capacitances of 1.98 , 2.39 and 3.99 F cm^{-2} .

The areal capacitance of core@shell MoCoNi-S@NiCo-OH electrode is higher than the sum of bare MoCoNi-S and NiCo-OH electrodes, which is attributed to synergic effects such as increased stability, electronic conductivity and electro-

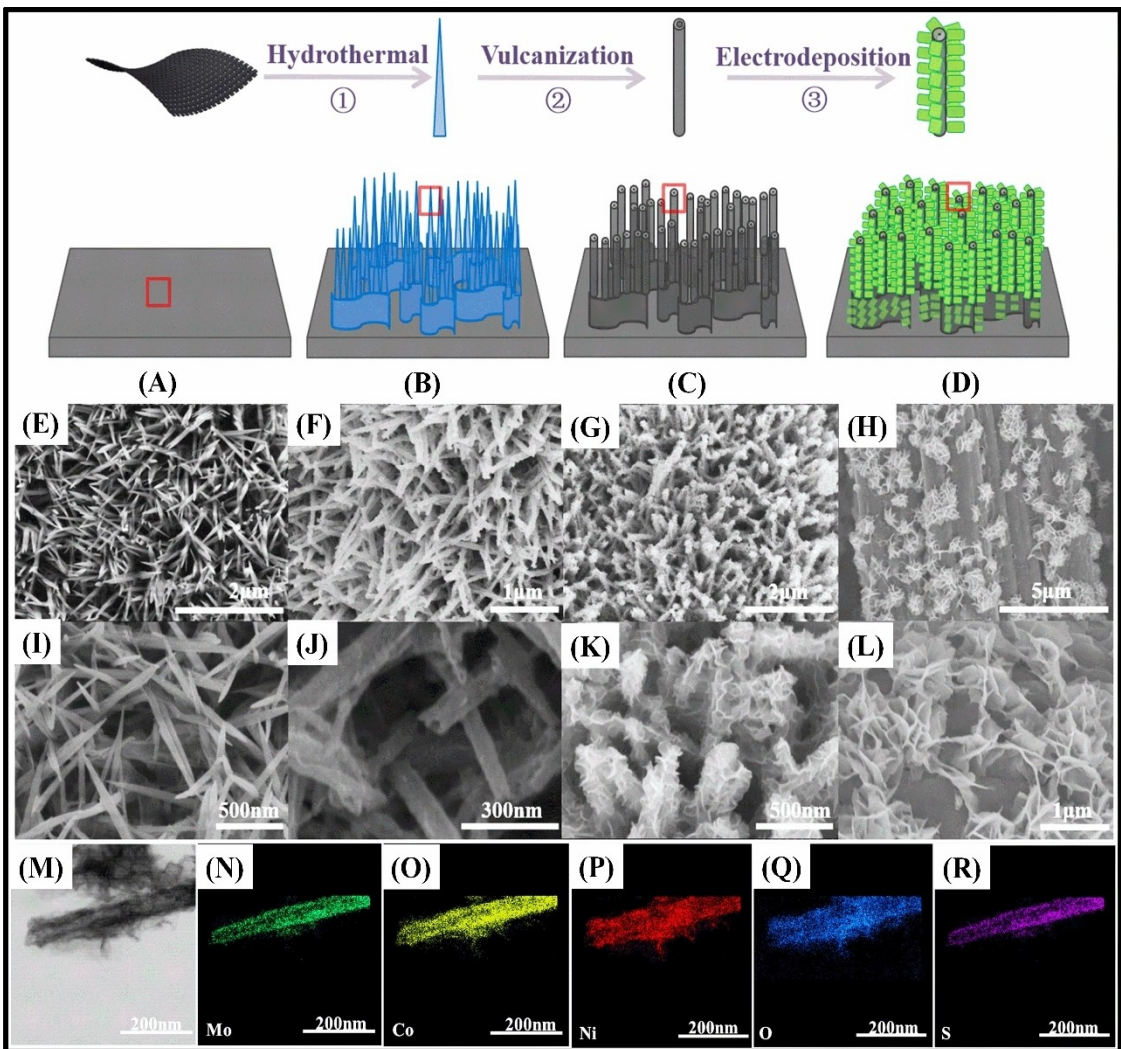


Figure 18. Schematic illustration of the formation of 3D core-shell nanoforest arrays. A) Bare carbon cloth substrate, B) MoCoNi precursor nanowire arrays (1 step), C) MoCoNi sulfide nanotube arrays (2 step), and D) 3D core-shell nanoforest arrays on CC (3 step). Typical SEM images of E) at different magnifications, I) MoCoNi precursor nanowire arrays, F) J) MoCoNi sulfide nanotube arrays, G) K) 3D core-shell nanoforest arrays, and H) L) NiCo nanosheet arrays on CC. (M) FEG-TEM image of 3D core-shell nanoforest arrays on CC and corresponding elemental mapping images of N) Mo, O) Co, P) Ni, Q) O, R) S. Reproduced from Ref. [64d] with permission. Copyright (2020) IOP Publishing.

lyte diffusion rates, with short ion/electron transport pathways, in addition to the presence of higher density of electrochemically active materials (NiCo-OH) in the same unit area, due to unique 3D nanopine forest array structure derived from tightly connected MoCoNi-S nanotubes and NiCo-OH ultrathin nanosheets. Additionally, both are pseudocapacitive materials such that the trimetallic sulfide core acts not only as porous scaffolds and conductive channels but also as a pseudocapacitive material, presenting multivalence sites of transition metal such as $\text{Co}^{2+}/\text{Co}^{3+}$, $\text{Ni}^{2+}/\text{Ni}^{3+}$ and $\text{Mo}^{4+}/\text{Mo}^{5+}/\text{Mo}^{6+}$, in addition to $\text{Co}^{2+}/\text{Co}^{3+}$ and $\text{Ni}^{2+}/\text{Ni}^{3+}$ active sites of NiCo-OH , thus endowing reversible ion-exchange, fast electron transport mechanisms and improved electrochemical stability.^[64d]

Ren *et al.*^[65] prepared the hierarchical petal-like NiFeCo-S@NiFeCo-TH heterogeneous ultrathin nanosheets *in-situ*, directly on nickel iron foam (NIF), by electro-oxidation combined with ion-exchange reaction (Figure 19A). A self-supporting

heterogeneous nanostructured electrode material with different architecture and morphology in comparison to the two materials reported above, was prepared taking advantage of the sulfide/hydroxide complimentary properties. Therefore, NiFeCo-S@NiFeCo-TH do not present a traditional core@shell heterostructure, but layered nanosheets of sulfides/hydroxides nanoparticles with different sizes (Figure 19E–19F). The specific areal capacitance delivered by NiFeCo-S@NiFeCo-TH/NIF was 9.56 F cm^{-2} at 10 mA cm^{-2} and rate capability of 83% from 10 to 100 mA cm^{-2} , with specific and areal charge capacities of 174 mAh g^{-1} and $973 \mu\text{Ah cm}^{-2}$ at 10 mA cm^{-2} , respectively, both with capacity retention of 68.4% at 100 mA cm^{-2} . These values were much interesting than that delivered by the electrodes made with the $\text{Ni}_2\text{S}_3@\text{FeS}@(\text{NiFe-DH})/\text{NIF}$ (5.34 F cm^{-2} and $564 \mu\text{Ah cm}^{-2}$ at 10 mA cm^{-2} , with 76% capacitance and 59% capacity retention at 100 mA cm^{-2}) and $\text{NiOOH}@(\text{FeOOH})/\text{NIF}$ (1.1 F cm^{-2} and $100 \mu\text{Ah cm}^{-2}$ at 10 mA cm^{-2} , with 80% capacitance and 70% capacity retention at 100 mA cm^{-2}).

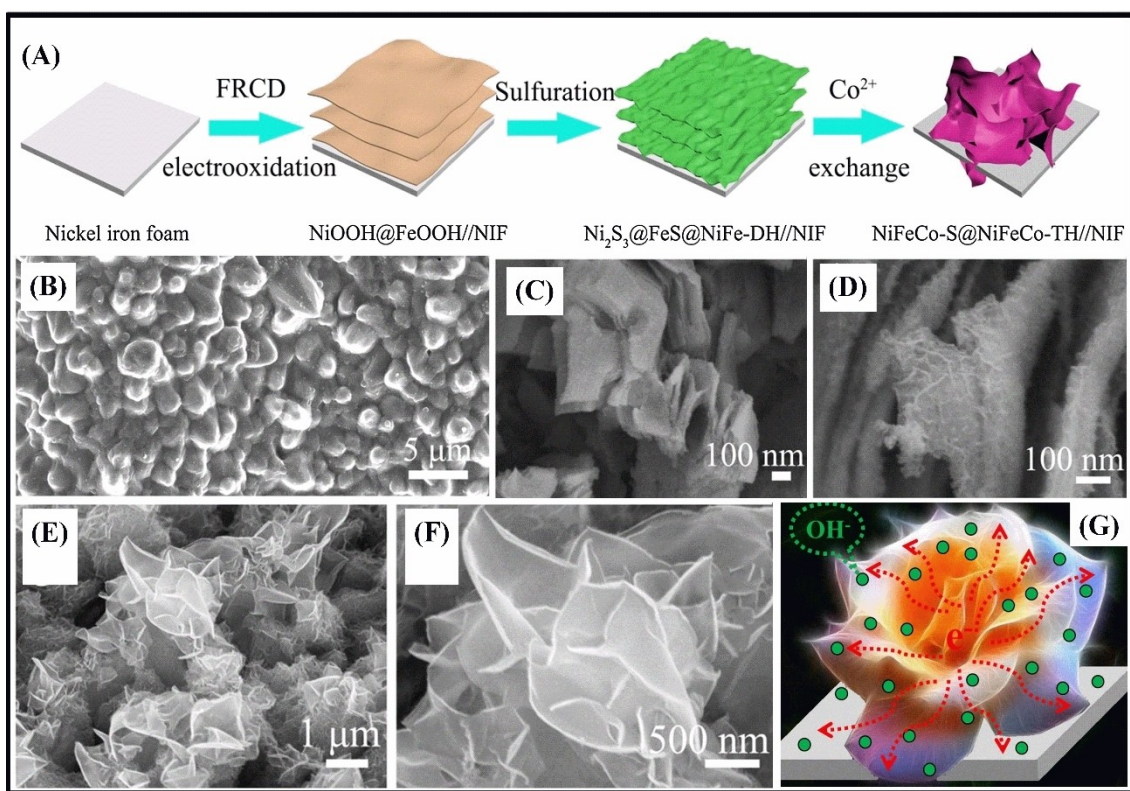


Figure 19. A) Schematic illustration of the synthesis of NiFeCo-S@NiFeCo-TH//NIF. SEM images of NIF (B), NiOOH@FeOOH//NIF (C), Ni_2S_3 @FeS@NiFe-DH//NIF (D), NiFeCo-S@NiFeCo-TH//NIF (E–F). G) Scheme illustrating the mechanism of electron and ion diffusion processes in NiFeCo-S@NiFeCo-TH//NIF. Reproduced from Ref. [65] with permission. Copyright (2020) Elsevier B.V.

NIF precursors (4.86 F cm^{-2} and $506 \mu\text{Ah cm}^{-2}$ at 10 mA cm^{-2} , with 63% capacitance and 35.6% capacity retention).

An all-solid-state NiFeCo-S@NiFeCo-TH/NIF//AC asymmetric supercapacitor was assembled with NiFeCo-S@NiFeCo-TH/NIF as the positive electrode and active carbon (AC) on NF as the negative electrode, and PVA-KOH gel as solid electrolyte and separator. NiFeCo-S@NiFeCo-TH/NIF//AC ASC displayed areal and specific capacity respectively of $1036 \mu\text{Ah cm}^{-2}$ and 57.2 mAh g^{-1} at 10 mA cm^{-2} , with rate capability of 68.3% at 150 mA cm^{-2} . It also presented a capacity retention of 90.1% after 4,000 cycles and coulombic efficiency of 96%. Additionally, the highest energy density of 56.3 Wh kg^{-1} was achieved at a power density of 543 W kg^{-1} whereas up to 28.3 Wh kg^{-1} was maintained at the highest power density of $3,500 \text{ W kg}^{-1}$.

The architecture and unique heterostructure of NiFeCo-S@NiFeCo-TH/NIF (Figure 19G) presents many additional synergistic effects, provided by the large surface area of cross-linked ultrathin petal-like nanosheets, and the presence of multi-metallic $\text{Ni}^{3+}/\text{Ni}^{2+}$, $\text{Co}^{3+}/\text{Co}^{2+}$ and $\text{Fe}^{3+}/\text{Fe}^{2+}$ redox couples in both core and shell structure. It is also important to emphasize the numerous edge sites and interfaces with strong affinity for OH^- present in the border areas between the Ni_3S_2 , FeS, CoNi_2S_4 , FeCoS_2 , and NiFeCo-OH crystalline phases. Finally, the increased mechanical and electrochemical stability, favorable electron-transfer rate and mechanical stability, larger electrode/electrolyte contact area, short ion/electron transport path-

lengths, facile and rapid OH^- adsorption/desorption should also be mentioned.

5.6. Trimetallic Sulfides as Shell Materials

Trimetallic sulfides having properties suited for both core and shell materials, hierarchical structures composed of carbon nanotube fibers (CNTF),^[64a] or nickel nanocone arrays (NCA)^[64c] core, and trimetallic sulfide shell were reported. Wang *et al.*^[64a] prepared a self-supported CNTF@MnNiCo-S multi-tripod nanotube array (NTA) electrode *via* a cost-effective hydrothermal process and subsequent anion-exchange, in which the CNTF core is uniformly covered by MnNiCo-S multi-tripod hollow and porous NTA (Figure 20A). The structure of such hollow multi-tripod nanotube arrays was confirmed by SEM (Figure 20B–20C) and TEM images (Figure 20D) of CNTF@MnNiCo-S, where the X-ray elemental mappings of Mn, Ni, Co and S recorded from an individual nanotube were also consistent with the composition of a trimetallic sulfide. The core@shell electrode delivered volumetric and areal capacitances of 2554.5 F cm^{-3} and 7.025 F cm^{-2} at 1 mA cm^{-2} , and 84.6% of capacitance retention at 10 mA cm^{-2} , which is about 2.5 and 5.4 times larger, respectively, than the volumetric capacitance delivered by CNTF@MnNiCo-O nanowire array and CNTF@NiCo-O core@shell material. Additionally, a fiber-shaped asymmetric supercapacitor (FASC) was assembled with CNTF@MnNiCo-S

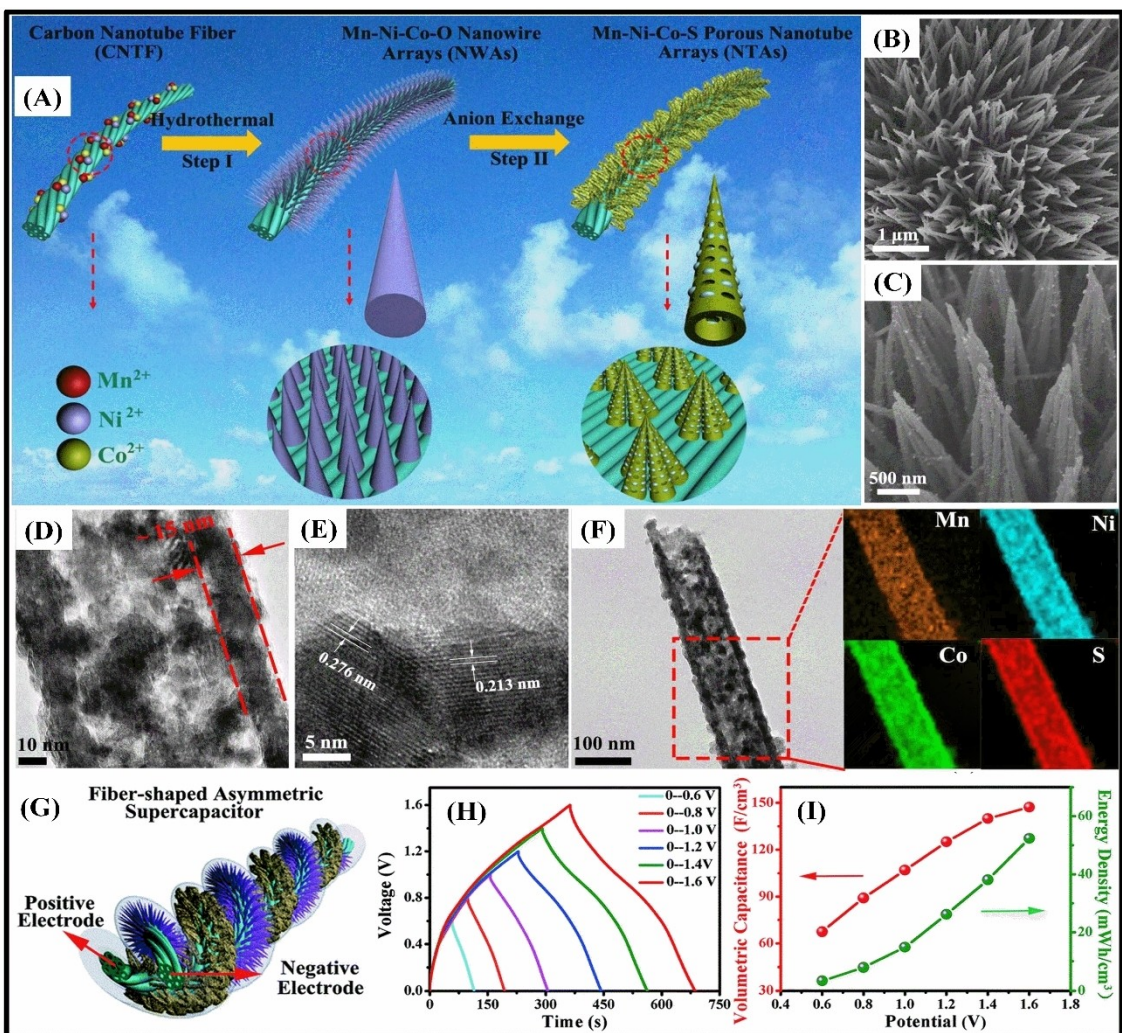


Figure 20. A) Scheme illustrating the synthesis of MNCS multi-tripod NTA. B, C) SEM images of MNCS NTA grown on CNTF at different magnifications. D) TEM images of MNCS nanotube structure. E) HRTEM image of the MNCS NTA structure. F) X-ray elemental mappings of Mn, Ni, Co and S recorded from an individual nanotube. G) Schematic illustration of the FASC device structure and H) the respective GCD curves collected from 0.4 to 1.6 V, at a current density of 2 mA cm^{-2} . I) Areal specific capacitance and energy density calculated based on the GCD curves obtained at 2 mA cm^{-2} . Reproduced from Ref. [64a] with permission. Copyright (2020) Royal Society of Chemistry.

multi-tripod NTAs as positive and vanadium nitride (VN) nanowires arrays on CNTF as negative electrodes (Figure 20G). The device achieved 147 F cm^{-3} and 405 mF cm^{-2} at 2 mA cm^{-2} , with 67.2% rate performance at 15 mA cm^2 (Figure 20H) and 92.9% capacitance retention after 5000 cycles, whereas the volumetric and areal energy densities were 52 mWh cm^{-3} and $144 \mu\text{Wh cm}^{-3}$ at the power density of 582 W cm^{-3} (Figure 20I).

Many other synergistic effects were attributed to the CNTF@MnNiCo-S multi-tripod NTA electrodes superior electrochemical performance due to the tight and complimentary interaction between the self-supporting CNTF core and MnNiCo-S hollow and porous multi-tripod NTA shell. The exceptionally high electrical conductivity resulted from the multi-metallic and multi-valence states and smaller band gap of the $\text{Mn}^{2+}/\text{Mn}^{3+}$, $\text{Ni}^{2+}/\text{Ni}^{3+}$ and $\text{Co}^{2+}/\text{Co}^{3+}/\text{Co}^{4+}$ redox couples forming MnSOH, NiSOH and CoSOH groups on the surface. These features promote reduced overall resistance, improve the electron collection rates and charge transport, enhance the

specific surface area, ion adsorption rate and the concentration of electroactive sites, decreasing the pathlengths for faster electrolyte ion and electron diffusion during the electrochemical reactions, as supported by the rough, multi-channeled, porous and hollow nanotube array structure.

Similarly to Wang *et al.*^[64a] who studied the properties of an electrode material made of a trimetallic sulfide shell on a highly conductive core and assembled a supercapacitor device, Rahimi, Shahrokhan and Hosseini^[64c] prepared NiCoFe-S directly on 3D nickel nanocone arrays (NCAs) by a facile two-steps electrodeposition to get NCA@NiCoFe-S on nickel plate (NP) (Figure 21A). First, well-ordered 3D NCAs core were vertically grown as clusters by electrodeposition of metallic Ni on NP surface (Figure 21B–21D). Then, an ultrathin NiCoFe-S nanosheets shell interconnected by sub-micron sized flower-like structures were grown on top of NCAs by a co-electrodeposition method (Figure 21E–21F). NCA@NiCoFe-S on NP electrode delivered a specific capacitance of $2,159.7 \text{ F g}^{-1}$ at

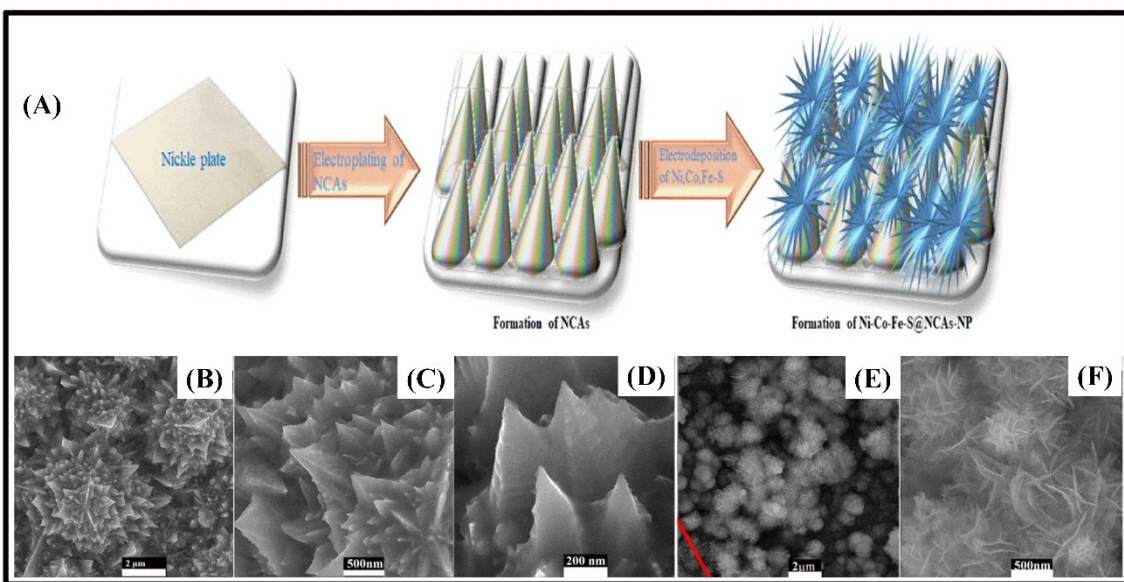


Figure 21. A) Scheme of the steps of fabrication of NCAs and Ni-Co-Fe-S@NCAs-NP. The FESEM images of as prepared B–D) NCAs and E–F) Ni-Co-Fe-S@NCAs-NP electrode. Reproduced from Ref. [64c] with permission. Copyright (2018) Elsevier B.V.

7 A g^{-1} , rate capability of 67.7% at 35 A g^{-1} , and capacitance retention of 92% after 1,000 cycles. In addition, NiCoFe-S were also directly grown by the same co-deposition method on NF and NP, in order to further explore the synergistic effects and benefits of the core@shell structuration in NCA@NiCoFe-S. NiCoFe-S/NF and NiCoFe-S/NP delivered almost 500 and 250 F g^{-1} of specific capacitance at 7 A g^{-1} , which is many times lower than the capacitance of the NCA@NiCoFe-S core@shell material. Moreover, the fabricated NiCoFe-S@NCAs/NP//rGO/NF ASC having NiCoFe-S@NCAs/NP as positive electrode and rGO on NF as the negative electrode, achieved 114 F g^{-1} at 0.2 A g^{-1} and retained about 26% of that capacitance at 10 A g^{-1} . The highest energy density achieved was 35.9 Wh kg^{-1} at a power density of 375 W kg^{-1} , and $7,500 \text{ W kg}^{-1}$ the highest power density achieved at 6.90 Wh kg^{-1} .

Similarly to CNTF@MnNiCo-S multi-tripod NTA electrodes,^[64a] the improved electrochemical performance of NCA@NiCoFe-S on NP can be attributed not only to the presence of reversible $\text{Mn}^{2+}/\text{Mn}^{3+}$, $\text{Ni}^{2+}/\text{Ni}^{3+}$ and $\text{Fe}^{2+}/\text{Fe}^{3+}$ redox pairs on the surface of the core@shell material, forming NiSOH, CoSOH and FeSOH groups, but also to the synergistic effects provided by structural features, such as the high specific surface area, availability and enhanced accessibility and ion-diffusion to the active sites. The highly conductive NCAs and the interconnected ultrathin trimetallic sulfide NiCoFe-S nanosheets complimentary properties also play relevant role, as well as the reduced thickness and lower accumulation of electrodeposited active materials on the surface of NF, due to the typical orientational features of the NCAs in comparison to NF and NP substrates.

6. Summary and Outlook

The appropriate choice of core@shell materials is the key to realize electrode materials with superior electrochemical performance. The core material must provide an excellent charge transfer rate and specific capacitance, and the shell must enhance the surface area in order to improve the accessibility of ions to the electroactive sites thus maximizing the charge diffusion rate. Thus, an excellent hierarchical 3D core@shell structure with high conductivity and surface area will not only facilitate the electrochemical processes but will also improve the charge transport and collection.

Therefore, bimetallic and trimetallic sulfides are excellent materials for the design of hierarchical 3D core@shell structures, once they can exhibit all those favorable features, in addition to much higher electrical conductivity than similar transition metal oxides (NiCo_2O_4),^[62] single component Ni- and Co-based oxides, and Ni- and Co-based sulfides,^[63] as well as a multifarious redox process assigned to their multi-metallic nature, thus providing exceptional specific capacity, power and energy density.

In fact, most of bimetallic sulfides used as core in the core@shell structures are Ni and Co spinels where the nickel and cobalt ions occupy tetrahedral and octahedral sites, respectively. Also, most of the shell materials in the bimetallic core@shell structures with metal sulfide core are metal oxides. The bimetallic sulfide cores have been prepared by hydrothermal method in several shapes such as nanowires, nanosheets, nanotubes, among others,^[35,42–43,59] but electrodeposition is the technique of choice when it comes to preparing tightly connected shell materials based on bimetallic sulfides directly on the core material, especially as high surface area nanosheets, due to the possibility of controlling the amount of deposited material by the amount of charge.

The trimetallic sulfides have unique and enhanced electrochemical properties in comparison to mono- and bimetallic sulfides, such as increased electron conductivity, facile anion exchange reactions, high density of redox sites and improved pseudocapacitive behavior. Notwithstanding, trimetallic sulfides also excel in comparison to trimetallic oxides exhibiting, for instance, higher electron conductivity, specific capacitance, electrochemical stability, and structural flexibility due to lower electronegativity of sulfur in comparison to oxygen, that leads to greatly improved electrochemical performances, especially when in core@shell materials, as reported in the work by Wang *et al.*^[64a] In addition, to overcome the instability of sulfides in aqueous electrolytes (especially in alkaline medium and during charge-discharge cycles), the core@shell nanostructuration^[64b] and the use of highly conductive substrates has been reported to enhance the cycling stability and current collection efficiency.^[67] In short, trimetallic sulfides present larger surface area, increased mechanical and electrochemical stabilities, abundant redox active sites, rapid transport of ions/electrons, enhanced conductivity, high coulombic efficiency and rich electrochemical properties, making them suitable for both, core and shell materials. In fact, the two highest specific capacitances presented by trimetallic sulfides core@shell materials are respectively $1,998 \text{ F g}^{-1}$ at 1 A g^{-1} ^[64d] and $2,159.7 \text{ F g}^{-1}$ at 7 A g^{-1} ^[64c] two surprisingly similar values.

Summarizing, the emerging trends in electrode materials for supercapacitor type energy storage devices are all based on sulfide-based multi-metallic 3D core@shell nanostructured materials with complex hierarchical structural features to optimize the density of redox sites as well as the ion and electron diffusion rates. Accordingly, the architectural design must meet with features design of materials in order to realize electrode materials whose properties are all suitable for real application in energy storage device technologies. In another perspective, researcher are eagerly seeking flexible enough materials for the development of supercapacitor/battery materials for wearable devices, self-charged energy storage devices, and microsupercapacitors.^[3b] To realize materials for future applications, the rational design of nanostructured materials encompassing sulfide-based core@shell connected to advanced 2D materials (such as graphene, MXene, black phosphorus, transition metal hydroxides, etc.), as well as other carbon materials such as CNTs and carbon cloth, seems to be a very promising strategy. Graphene and carbon cloth are highly conducting, light-weight, tough and flexible enough materials for application as substrates/current collectors of flexible/wearable energy devices, where multi-metallic sulfide-based core@shell materials play a key role as electroactive materials for realization of high performance, portable and flexible energy storage devices in the way towards a more advanced and sustainable society.

Acknowledgments

This work was supported by the São Paulo Research Foundation (FAPESP) 2018/21489-1, 2017/13137-5, 2014/50867-3 and 2013/

24725-4) and the National Council for Scientific and Technological Development (CNPq 303137/2016-9, 311847-2018-8, 401581/2016-0, 408222/2016-6), in addition to the fellowships granted to J.M.G. (FAPESP 2018/16896-7).

Conflict of Interest

The authors declare no conflict of interest.

Keywords: sulfides · supercapacitors · core@shell materials, energy storage

- [1] J. P. Cheng, W. D. Wang, X. C. Wang, F. Liu, *Chem. Eng. J.* **2020**, *393*, 124747.
- [2] C. Zhu, P. Yang, D. Chao, W. Mai, H. J. Fan, *ChemNanoMat* **2015**, *1*, 458–476.
- [3] a) J. M. Gonçalves, M. I. da Silva, H. E. Toma, L. Angnes, P. R. Martins, K. Araki, *J. Mater. Chem. A* **2020**, *8*, 10534–10570; b) J. M. Gonçalves, M. N. T. Silva, K. K. Naik, P. R. Martins, D. P. Rocha, E. Nossol, R. A. A. Munoz, L. Angnes, C. S. Rout, *J. Mater. Chem. A* **2021**, *9*, 3095–3124.
- [4] J. Theerthagiri, R. A. Senthil, P. Nithyadharseeni, S. J. Lee, G. Durai, P. Kuppusami, J. Madhavan, M. Y. Choi, *Ceram. Int.* **2020**, *46*, 14317–14345.
- [5] A. S. Aliyev, M. Elrouby, S. F. Cafarova, *Mat Sci Semicon Proc* **2015**, *32*, 31–39.
- [6] J. Theerthagiri, R. A. Senthil, B. Senthilkumar, A. Reddy Polu, J. Madhavan, M. Ashokkumar, *J. Solid State Chem.* **2017**, *252*, 43–71.
- [7] Y.-P. Gao, K.-J. Huang, *Chem. Asian J.* **2017**, *12*, 1969–1984.
- [8] a) C.-H. Lai, M.-Y. Lu, L.-J. Chen, *J. Mater. Chem.* **2012**, *22*, 19–30; b) X. Rui, H. Tan, Q. Yan, *Nanoscale* **2014**, *6*, 9889–9924; c) X.-Y. Yu, L. Yu, X. W. Lou, *Adv. Energy Mater.* **2016**, *6*, 1501333; d) J. Theerthagiri, K. Karuppasamy, G. Durai, A. U. H. S. Rana, P. Arunachalam, K. Sangeetha, P. Kuppusami, H.-S. Kim, *Nanomaterials* **2018**, *8*, 256.
- [9] P. Kulkarni, S. K. Nataraj, R. G. Balakrishna, D. H. Nagaraju, M. V. Reddy, *J. Mater. Chem. A* **2017**, *5*, 22040–22094.
- [10] X. Y. Yu, X. W. Lou, *Adv. Energy Mater.* **2018**, *8*, 1701592.
- [11] P. Geng, S. Zheng, H. Tang, R. Zhu, L. Zhang, S. Cao, H. Xue, H. Pang, *Adv. Energy Mater.* **2018**, *8*, 1703259.
- [12] G. Wang, L. Zhang, J. Zhang, *Chem. Soc. Rev.* **2012**, *41*, 797–828.
- [13] S. Das, J. Pérez-Ramírez, J. Gong, N. Dewangan, K. Hidajat, B. C. Gates, S. Kawi, *Chem. Soc. Rev.* **2020**, *49*, 2937–3004.
- [14] a) W. Wu, P. Xia, Y. Xuan, R. Yang, M. Chen, D. Jiang, *Nanotechnology* **2020**, *31*, 405705; b) J. Chang, S. Zang, Y. Wang, C. Chen, D. Wu, F. Xu, K. Jiang, Z. Bai, Z. Gao, *Electrochim. Acta* **2020**, *353*, 136501.
- [15] W. Fu, C. Zhao, W. Han, Y. Liu, H. Zhao, Y. Ma, E. Xie, *J. Mater. Chem. A* **2015**, *3*, 10492–10497.
- [16] P. Zhang, J. Zhou, W. Chen, Y. Zhao, X. Mu, Z. Zhang, X. Pan, E. Xie, *Chem. Eng. J.* **2017**, *307*, 687–695.
- [17] Y. Gogotsi, R. M. Penner, *ACS Nano* **2018**, *12*, 2081–2083.
- [18] N. R. Chodankar, H. D. Pham, A. K. Nanjundan, J. F. S. Fernando, K. Jayaramulu, D. Golberg, Y.-K. Han, D. P. Dubal, *Small* **2020**, *16*, 2002806.
- [19] Y. Jiang, J. Liu, *Energy Environ. Mater.* **2019**, *2*, 30–37.
- [20] a) P. Simon, Y. Gogotsi, B. Dunn, *Science* **2014**, *343*, 1210; b) T. Brousse, D. Bélanger, J. W. Long, *J. Electrochem. Soc.* **2015**, *162*, A5185–A5189.
- [21] Z. Wang, H. Jia, Y. Cai, C. Li, X. Zheng, H. Liang, J. Qi, J. Cao, J. Feng, *Chem. Eng. J.* **2020**, *392*, 123890.
- [22] G. Liu, B. Wang, T. Liu, L. Wang, H. Luo, T. Gao, F. Wang, A. Liu, D. Wang, *J. Mater. Chem. A* **2018**, *6*, 1822–1831.
- [23] F. Song, Q. Chen, Y. Li, Y. Li, L. Zhang, *Chem. Eng. J.* **2020**, *390*, 124561.
- [24] J. Shi, X. Li, G. He, L. Zhang, M. Li, J. Mater. Chem. A **2015**, *3*, 20619–20626.
- [25] A. G. Tabrizi, N. Arsalani, Z. Naghshbandi, L. S. Ghadimi, A. Mohammadi, *Int. J. Hydrogen Energy* **2018**, *43*, 12200–12210.
- [26] Y. Lv, Z. Guo, A. Liu, H. Che, J. Mu, X. Zhang, Y. Bai, Z. Zhang, G. Wang, *Ceram. Int.* **2017**, *43*, 12948–12956.
- [27] S. Liu, Y. Yin, M. Wu, K. S. Hui, K. N. Hui, C.-Y. Ouyang, S. C. Jun, *Small* **2019**, *15*, 1803984.
- [28] L. Cheng, Y. Hu, L. Ling, D. Qiao, S. Cui, Z. Jiao, *Electrochim. Acta* **2018**, *283*, 664–675.

- [29] Q. Shi, Q. Zhang, Q. Zang, Y. Yang, Z. Xiao, L. Zong, K.-P. Wang, L. Wang, *J. Power Sources* **2020**, *475*, 228631.
- [30] Q. Liu, X. Hong, X. You, X. Zhang, X. Zhao, X. Chen, M. Ye, X. Liu, *Energy Storage Mater.* **2020**, *24*, 541–549.
- [31] Z. Gao, C. Chen, J. Chang, L. Chen, P. Wang, D. Wu, F. Xu, K. Jiang, *Chem. Eng. J.* **2018**, *343*, 572–582.
- [32] a) S. Liu, S. C. Jun, *J. Power Sources* **2017**, *342*, 629–637; b) L. Shen, L. Yu, H. B. Wu, X.-Y. Yu, X. Zhang, X. W. Lou, *Nat. Commun.* **2015**, *6*, 6694.
- [33] a) R. Li, S. Wang, Z. Huang, F. Lu, T. He, *J. Power Sources* **2016**, *312*, 156–164; b) J. Liang, M. Li, Y. Chai, M. Luo, L. Li, *J. Power Sources* **2017**, *362*, 123–130.
- [34] G. Yu, X. Xie, L. Pan, Z. Bao, Y. Cui, *Nano Energy* **2013**, *2*, 213–234.
- [35] Y. Zhao, X. He, R. Chen, Q. Liu, J. Liu, D. Song, H. Zhang, H. Dong, R. Li, M. Zhang, J. Wang, *Appl. Surf. Sci.* **2018**, *453*, 73–82.
- [36] S. Cheng, T. Shi, Y. Huang, X. Tao, J. Li, C. Cheng, G. Liao, Z. Tang, *Ceram. Int.* **2017**, *43*, 2155–2164.
- [37] A. Singh, S. K. Ojha, M. Singh, A. K. Ojha, *Electrochim. Acta* **2020**, *349*, 136349.
- [38] T. Xing, Y. Ouyang, Y. Chen, L. Zheng, H. Shu, C. Wu, B. Chang, X. Wang, *Electrochim. Acta* **2020**, *351*, 136447.
- [39] B. Shi, B. Saravanan Kumar, W. Wei, G. Dong, S. Wu, X. Lu, M. Zeng, X. Gao, Q. Wang, G. Zhou, J.-M. Liu, K. Kempa, J. Gao, *J. Alloys Compd.* **2019**, *790*, 693–702.
- [40] X. Chang, W. Li, Y. Liu, M. He, X. Zheng, J. Bai, Z. Ren, *J. Colloid Interface Sci.* **2019**, *538*, 34–44.
- [41] X. Liu, Z. Wu, Y. Yin, *Chem. Eng. J.* **2017**, *323*, 330–339.
- [42] X. Mao, Y. Wang, C. Xiang, D. Zhan, H. Zhang, E. Yan, F. Xu, X. Hu, J. Zhang, L. Sun, Y. Zou, *J. Alloys Compd.* **2020**, *844*, 156133.
- [43] H.-B. Li, G.-F. Xiao, H.-Y. Zeng, X.-J. Cao, K.-M. Zou, S. Xu, *Electrochim. Acta* **2020**, *352*, 136500.
- [44] Q. Zhou, J. Huang, C. Li, Z. Lv, H. Zhu, G. Hu, *New J. Chem.* **2019**, *43*, 5904–5913.
- [45] S. Zhou, Y. Liu, M. Yan, L. Sun, B. Luo, Q. Yang, W. Shi, *Electrochim. Acta* **2020**, *349*, 136337.
- [46] Y. Lv, A. Liu, Z. Shi, H. Che, J. Mu, Z. Guo, X. Zhang, *Chem. Eng. J.* **2018**, *349*, 397–407.
- [47] D. Han, J. Wei, Y. Zhao, Y. Shen, Y. Pan, Y. Wei, L. Mao, *Inorg. Chem. Front.* **2020**, *7*, 1428–1436.
- [48] P. Zhang, H. He, *Appl. Surf. Sci.* **2019**, *497*, 143725.
- [49] L. Zhou, Y. He, C. Jia, V. Pavlinek, P. Saha, Q. Cheng, *Nanomaterials* **2017**, *7*.
- [50] L. G. Beka, X. Li, X. Xia, W. Liu, *Diamond Relat. Mater.* **2017**, *73*, 80–86.
- [51] J. Zhang, H. Guan, Y. Liu, Y. Zhao, B. Zhang, *Electrochim. Acta* **2017**, *258*, 182–191.
- [52] B. S. Soram, I. S. Thangjam, J. Y. Dai, T. Kshetri, N. H. Kim, J. H. Lee, *Chem. Eng. J.* **2020**, *395*, 125019.
- [53] X. Wang, L. Xu, K. Song, R. Yang, L. Jia, X. Guo, X. Jing, J. Wang, *Colloids Surf. A* **2019**, *570*, 73–80.
- [54] K. Le, M. Gao, W. Liu, J. Liu, Z. Wang, F. Wang, V. Murugadoss, S. Wu, T. Ding, Z. Guo, *Electrochim. Acta* **2019**, *323*, 134826.
- [55] F. Ma, X. Dai, J. Jin, N. Tie, Y. Dai, *Electrochim. Acta* **2020**, *331*, 135459.
- [56] K. Yu, W. M. Tang, J. Dai, *Phys. Status Solidi A* **2018**, *215*, 1800147.
- [57] C. Cheng, X. Zhang, C. Wei, Y. Liu, C. Cui, Q. Zhang, D. Zhang, *Ceram. Int.* **2018**, *44*, 17464–17472.
- [58] L. Ma, T. Chen, S. Li, P. Gui, G. Fang, *Nanotechnology* **2019**, *30*, 255603.
- [59] K. Song, X. Chen, R. Yang, B. Zhang, X. Wang, P. Liu, J. Wang, *Chem. Eng. J.* **2020**, *390*, 124175.
- [60] J. Zhu, S. Tang, J. Wu, X. Shi, B. Zhu, X. Meng, *Adv. Energy Mater.* **2017**, *7*, 1601234.
- [61] J. Wang, J. Polleux, J. Lim, B. Dunn, *J. Phys. Chem. C* **2007**, *111*, 14925–14931.
- [62] H. Chen, J. Jiang, L. Zhang, H. Wan, T. Qi, D. Xia, *Nanoscale* **2013**, *5*, 8879–8883.
- [63] T.-F. Yi, J.-J. Pan, T.-T. Wei, Y. Li, G. Cao, *Nano Today* **2020**, *33*, 100894.
- [64] a) X. Wang, Q. Zhang, J. Sun, Z. Zhou, Q. Li, B. He, J. Zhao, W. Lu, C.-p. Wong, Y. Yao, *J. Mater. Chem. A* **2018**, *6*, 8030–8038; b) J. S. Sanchez, A. Pendashteh, J. Palma, M. Anderson, R. Marcilla, *J. Mater. Chem. A* **2019**, *7*, 20414–20424; c) S. Rahimi, S. Shahrokhian, H. Hosseini, *J. Electroanal. Chem.* **2018**, *810*, 78–85; d) M. Lv, X. Zhang, F. Wang, T. Yu, H. Lv, Y. Zhai, Y. Shen, G. Lv, *Nanotechnology* **2020**, *31*, 225603.
- [65] X. Ren, Y. Zhou, Y. Du, Y. Jiang, Y. Chen, J. Wan, F. Ma, *Appl. Surf. Sci.* **2020**, *514*, 145951.
- [66] W. Zhao, G. Yan, Y. Zheng, B. Liu, D. Jia, T. Liu, L. Cui, R. Zheng, D. Wei, J. Liu, *J. Colloid Interface Sci.* **2020**, *565*, 295–304.
- [67] H. Li, X. Chen, E. Zalnezhad, K. N. Hui, K. S. Hui, M. J. Ko, *J. Ind. Eng. Chem.* **2020**, *82*, 309–316.

Manuscript received: January 18, 2021

Revised manuscript received: March 1, 2021

Accepted manuscript online: March 4, 2021

Version of record online: March 26, 2021